



# Region-edge-based active contours driven by hybrid and local fuzzy region-based energy for image segmentation



Jiangxiong Fang <sup>a,b,\*</sup>, Huaxiang Liu <sup>a</sup>, Liting Zhang <sup>a</sup>, Jun Liu <sup>a</sup>, Hesheng Liu <sup>b,\*</sup>

<sup>a</sup> State Key Laboratory of Nuclear Resources and Environment, East China Institute of Technology, Nanchang, Jiangxi 330013, China

<sup>b</sup> School of Mechanical and Electrical Engineering, Nanchang University, Nanchang, Jiangxi 330031, China

## ARTICLE INFO

### Article history:

Received 26 October 2018

Received in revised form 21 June 2020

Accepted 23 August 2020

Available online 1 September 2020

### Keywords:

Hybrid energy

Active contour

Intensity inhomogeneity

Edge energy

## ABSTRACT

This paper raises a region-edge-based active contour driven by the hybrid and local fuzzy region-based energy to segment images with high noise and intensity inhomogeneity. The energy functional consists of region energy and edge energy. The region energy is made up of hybrid fuzzy region term and local fuzzy region term. Its aim is to motivate initial contour to move toward the exact object boundary. What's more, it is proved to be convex and ensures the segmentation results independent of initialization. The hybrid fuzzy region term can balance the importance of the object and background while the local fuzzy region term by incorporating spatial and local information can decrease the effect of intensity inhomogeneity in given images. The edge energy is used to regularize the pseudo level set function (LSF) and maintain the appearance of the smoothness during the curve evolution. Inspired by the fuzzy energy-based active contour (FEAC), a more direct and simpler method is developed to calculate the difference between the old and new energy functions to update the pseudo LSF during the curve evolution. Experimental results on synthetic and real images with high noise and intensity inhomogeneity show that the proposed model can obtain better performance than the state-of-the-art active contour models. The code is available at: <https://github.com/fangchj2002/HLFRA>.

© 2020 Elsevier Inc. All rights reserved.

## 1. Introduction

Image segmentation plays a fundamental and important role in image analysis and computer vision. Its purpose is to divide a given image into several parts where each part is homogeneous as the aspect of a certain characteristic, i.e. intensity, color, and texture [1,2]. In recent years, numerous image segmentation algorithms have been proposed to enhance the efficiency of image segmentation. Variational model based on partial differential equations (PDE) [3–5], whose objective function consists of the region and boundary information, has become one of the most effective algorithms in the field of image segmentation. However, developing an efficient segmentation algorithm is still an essential and difficult task due to the complexity of the images.

“Active contour models” (ACMs) [6] have become an efficient framework in the field of image segmentation. They can mainly fall into the “edge-based ACMs” [4,5] and “region-based ACMs” [6–8]. The “edge-based ACMs” [2,3] use gradient information to guide the evolving contour to move toward the object boundaries. But these models are sensitive to the initial contours and cannot extract the objects with weak or blurred boundaries. In the “region-based ACMs” [4–8], the energy

\* Corresponding authors.

E-mail addresses: [fangchj2002@ecut.edu.cn](mailto:fangchj2002@ecut.edu.cn) (J. Fang), [hsliu@vip.163.com](mailto:hsliu@vip.163.com) (H. Liu).

function is formulated based on image region information, e.g. intensity, color, and texture, where the energy is minimized when the evolving curves reach at the real object boundary. In this paper, we mainly discuss the region-based ACMs. In these models, a zero “level set function” (LSF) is used to express the contour curve, and is also called signed distance function. As an especial example of Mumford-Shah (M-S) model [8], Chan-Vese model [6] is one of the most well-known region-based ACMs. The model makes use of the difference between the inside and outside average intensities to spur the motion of the evolution curve toward the boundaries instead of image gradient. However, these region-based ACMs have three disadvantages: (1) They cannot deal with intensity inhomogeneity in images, e.g. noise, blurred boundary, and low contrast. (2) The periodical re-initialization of the LSF, which is used to maintain the sign distance information of the LSF, greatly increases the amount of computation. (3) The non-convex energy function with the regularization term makes the evolution curves stuck in local optima.

In order to obtain better segmentation performance for segmenting images with intensity inhomogeneity, many improved Chan-Vese models [7–10] were proposed by incorporating local image information into the energy functional. A piecewise smooth (PS) model proposed by Vese and Chan [9] was extended to multiphase image segmentation based on two level set functions. But its computational cost was very high. In [10,11], Li et al. proposed a “local binary fitting” (LBF) model using a convolutional kernel function to extract local image information. Its aim is to utilize local image information with spatially varying weight by controlling a scalable parameter to extract image features. A local image fitting (LIF) model [12] was constructed by introducing a fitting image with a Gaussian kernel function to extract the local image information. Many improved fitted energy models are based on different local fitted images, e. g. “local hybrid image fitting energy” (LHIF) model [13], “local likelihood image fitting” (LLIF) energy model [14], and local cosine fitting energy [15]. An active contour model driven by “local pre-fitting energy” (LPE) [16] was formulated based on the average image intensities in local region before the evolution of curve. The LPE model takes less running time, but it is difficult to adaptively extract the object local features. Local statistical region-based ACMs [17–20] based on the Chan-Vese model via Gaussian function were introduced to construct the energy function. A variational model [21] was proposed to handle intensity inhomogeneity with the multiplicative noise. In addition, to avoid the periodical re-initialization of the LSF, a “distance regularized level set evolution” (DRLSE) model [22,23] was designed by introducing a penalty term to smooth the LSF and maintain the distance feature during the curve evolution. Zhang et al. [12] used a Gaussian filter to smooth the LSF and maintain the characteristic of the LSF during iterations.

To solve the minimization problem of the energy functional in the region-based ACMs, which causes the segmentation results sensitive to the initial conditions, massive methods based on convex optimization have been designed to obtain global minimum. A “fuzzy energy-based active contour” (FEAC) [24] was formulated by incorporating fuzzy sets into the ACM. From then on, many improved FEAC-based models by incorporating local image information into region-based ACMs were proposed. The local energy functional in the global and local FEAC models [25–27] (GL-FEAC) was constructed by incorporating both local spatial and intensity information into ACM, which was used to decrease the effect of intensity inhomogeneity in given images. Image features, such as kernel metric [28] and shape prior [29], were also fused into the FEAC model to improve the segmentation performance. However, these models without the regularization term lead to the non-smoothness of the evolution curve and cannot maintain the distance feature of the pseudo LSF. In addition, updating the degree of membership by computing the changed values of pixel-by-pixel energy function during the curve evolution greatly increases the computational complexity. More importantly, they may suffer from a boundary leakage problem when the segmented images include weak edges and low contrast.

In this paper, to solve these problems mentioned above, inspired by the FEAC model [24], we proposed a novel Hybrid and Local Fuzzy Region-edge based Active contour model for image segmentation, called HLFRA. The HLFRA model includes two parts. In the first part, the region energy is designed to guide the evolving curve to move toward the object boundaries. The region energy includes a hybrid fuzzy region term and a local fuzzy region term, where two terms have been proved to be strictly convex and make the results independent of initialization. In the second part, the edge energy with a regularization term and a penalty term is used to ensure the accurate detection of the objects. The HLFRA model is tested on synthetic and real images by adding different types of noises, and the results show that the proposed model can obtain better performance and take less running time than the popular region-based ACMs. Our main contributions are as follows:

- 1) The region energy including a hybrid fuzzy region term and a local fuzzy region term is proved to be convex, which ensures the segmentation results independent of initialization. The hybrid fuzzy region term is constructed by incorporating local and global image average information to approximate inhomogeneity intensity. Meanwhile, the local fuzzy region term by incorporating spatial and local image information can reduce the effect of intensity inhomogeneity.
- 2) To maintain the appearance and smoothness of the contour curve in the proposed model, the edge energy is developed to regularize the pseudo LSF and maintain the appearance of the smoothness during evolution.
- 3) To simplify the calculating process and improve the computing efficiency, a more direct and simpler method by computing the energy difference between the new energy and the old one is developed to update the degree of membership during evolution.

The remainder of this paper is organized as follows. Previous work related to the HLFRA model is described in Section 2. Section 3 describes the proposed model, including formulation of region energy, formulation of edge energy, numerical

approximation, and the detailed description steps. Section 4 depicts the experimental results including experimental results on synthetic and real images, robustness to initialization, comparison with the popular region-based ACMs, and the effect of parameters. Finally, the conclusion is given in Section 5.

## 2. Previous work

### 2.1. Chan-Vese model

The Chan-Vese model [6] divides the image into two disjoint regions with initial contour  $C$ . Its energy functional is formulated based on the intensity difference between the inside and outside regions around the closed curve  $C$ . Let  $I(x) : \Omega \rightarrow R^2$  be a segmented image in the image domain  $\Omega$ , the energy functional is defined as:

$$E^{CV}(C, l_1, l_2) = \lambda_1 \int_{Out(C)} (I(x) - l_1)^2 dx + \lambda_2 \int_{In(C)} (I(x) - l_2)^2 dx + \mu \cdot len(C) \quad (1)$$

where  $\lambda_1$ ,  $\lambda_2$ , and  $\mu$  are three positive weighting parameters,  $len(C)$  is the length of the contour  $C$ ,  $In(C)$  and  $Out(C)$  denote two regions inside  $C$  and outside  $C$ , respectively, and their corresponding average intensities are presented as  $l_1$  and  $l_2$ .

To solve the minimization energy, a zero level set based on the Lipschitz function  $\phi(x)$  is used to express the contour curve  $C$ . The LSF  $\phi(x)$  is defined as follows:

$$\begin{cases} \phi(x) > 0 & \text{if } x \in In(C) \\ \phi(x) = 0 & \text{if } x \in On(C) \\ \phi(x) < 0 & \text{if } x \in Out(C) \end{cases} \quad (2)$$

Therefore, the energy functional  $E^{CV}(l_1, l_2, C)$  defined in Eq. (1) is expressed as:

$$E_{\varepsilon}^{CV}(l_1, l_2, \phi) = \lambda_1 \int_{\Omega} (I(x) - l_1)^2 H_{\varepsilon}(\phi) dx + \lambda_2 \int_{\Omega} (I(x) - l_2)^2 (1 - H_{\varepsilon}(\phi)) dx + \mu \cdot \int_{\Omega} \delta_{\varepsilon}(\phi) |\nabla \phi| dx \quad (3)$$

where  $H_{\varepsilon}(x) = 1/2 \cdot [1 + 2/\pi \cdot \arctan(x/\varepsilon)]$  is the Heaviside function, and  $\delta_{\varepsilon}(x) = \frac{dH_{\varepsilon}(x)}{dx}$  is the Dirac delta function.

Then, the variational method based on the Euler-Lagrange equations is to obtain minimum energy functional  $E^{CV}$ , and the gradient descent algorithm is used to update the LSF. However, the Chan-Vese model cannot accurately handle the detection of objects for the images with severe intensity inhomogeneity.

### 2.2. LBF model

Li et al. [9] proposed a local binary fitting (LBF) model by incorporating local image information, which was implemented by a Gaussian kernel function. The model is used to deal with intensity inhomogeneity in images. The energy function in the LBF model is written as:

$$E^{LBF}(\phi, h_1, h_2) = \sum_{i=1}^2 \lambda_i \int_{\Omega} \int_{\Omega} K_r(x-y) (I(y) - h_i(x))^2 H_i(\phi) dy dx \quad (4)$$

where  $K_r$  is a Gaussian kernel function with standard deviation  $r$ ,  $y$  is a spatial pixel independent of  $x$ , two smooth functions  $h_1$  and  $h_2$  are used to estimate the local intensities inside and outside the contour  $C$ , respectively.

The energy function in the LBF model by adding a penalizing term can avoid the re-initialization procedure and extract the desirable objects from the inhomogeneous images. But the model still needs four convolution operators during each iteration, which increases the computational cost. In addition, the segmentation results are highly dependent on the initial localization.

### 2.3. FEAC model

To obtain global convex energy function, Krinidis and Chatzis [24] proposed a FEAC model by incorporating the fuzzy sets into ACM. Different from the popular ACMs, the FEAC model uses a 0.5 level set as the evolution curve. The pseudo LSF is defined as:

$$\begin{cases} u(x) = 0.5 & I(x) \in C \\ u(x) > 0.5 & I(x) \in In(C) \\ u(x) < 0.5 & I(x) \in out(C) \end{cases} \quad (5)$$

where  $I(x)$  is an input image, and  $In(C)$  and  $Out(C)$  denote the regions inside and outside the contour curve  $C$ , respectively.

By introducing the pseudo LSF defined in Eq. (5), which divides an input image into two regions, the energy function is expressed as:

$$E(C, l_1, l_2) = \eta \cdot \text{Len}(C) + \lambda_1 \int_{\Omega} [u(x)]^m (I(x) - l_1)^2 dx + \lambda_2 \int_{\Omega} [1 - u(x)]^m (I(x) - l_2)^2 dx \quad (6)$$

where the constants  $\eta \geq 0$ ,  $\lambda_1, \lambda_2 > 0$  are three fixed parameters,  $l_1$  and  $l_2$  are average intensities inside and outside the contour  $C$ , respectively, and  $m$  is an exponent. Two average intensities are defined as:

$$l_1 = \frac{\int_{\Omega} [u(x)]^m I(x) dx}{\int_{\Omega} [u(x)]^m dx}, \quad l_2 = \frac{\int_{\Omega} [1 - u(x)]^m I(x) dx}{\int_{\Omega} [1 - u(x)]^m dx} \quad (7)$$

To obtain the updating variable, keeping the parameters  $l_1$  and  $l_2$  fixed and minimizing the energy function  $E(C, l_1, l_2)$  in Eq. (6) with respect to  $u$ , the degree of membership is written as:

$$u(x) = \frac{1}{1 + \left( \frac{\lambda_1 (I(x) - l_1)^2}{\lambda_2 (I(x) - l_2)^2} \right)^{\frac{1}{m-1}}} \quad (8)$$

Specifically, in the computing process, the first step is to calculate the fuzzy membership for a certain pixel  $x$  in the image using Eq. (8). Then, the new fuzzy membership is updated according to the changed values of the energy function caused by the change of the fuzzy membership. If the changed value is negative, the fuzzy membership is updated. Otherwise, the old one is kept. In the third step, the above process is repeated for the whole image domain, and one iteration is finished. Finally, the iterative process continues until the total energy is unchanged.

### 3. The proposed model

In this section, we present the formulation of the proposed model in detail, and the segmentation framework is shown in Fig. 1. As the same to the FEAC model [24], the evolving contour  $C$  presented as a 0.5 level set of a LSF  $u(x) = 0.5$  separates the image domain  $\Omega$  into two adjacent regions: inside region  $C_{in}(u > 0.5)$  and outside region  $C_{out}(u < 0.5)$ . The energy functional  $F$  is composed of two parts: region energy  $F^R$  and edge energy  $F^E$ . The region energy motivates the initial pseudo LSF (evolving curve) to move toward the object while the edge energy is used to accurately detect exact boundary. The energy function  $F$  is defined as follows:

$$F(u) = F^R(u) + F^E(u) \quad (9)$$

#### 3.1. Formulation of region energy

The real-world images usually appear intensity inhomogeneity which causes blurring of the image edges between adjacent regions. In general, the model describing intensity inhomogeneity in a given image domain  $\Omega$  is written as:

$$I(x) = b(x)J(x) + n(x) \quad (10)$$

where  $I(x)$  is an intensity value of the observed image,  $b(x)$  is a smoothly changing bias field which reflects intensity inhomogeneity,  $J(x)$  is a real intensity value of the inhomogeneity-free image, and  $n(x)$  is additive noise. The additive noise  $n(x)$  is small enough, so we can omit it. Thus, the observed image  $I(x)$  can be simplified as  $I(x) \approx b(x)J(x)$ .

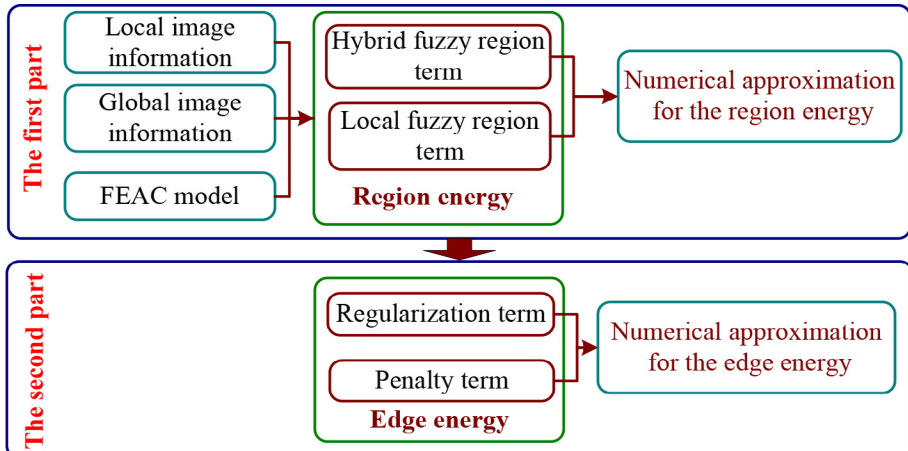


**Fig. 1.** Segmentation framework of the proposed model.

To approximate intensity inhomogeneity in given images, a local region with spatial information is used to estimate pixel intensities. For pixel  $x$  in the image domain  $\Omega \in R^2 \setminus \text{MERGEFORMAT}$ , the spatial pixel  $y$  centered at  $x$  in a small region  $\Omega_x$ , i.e. the rectangle or circle region, two average intensities  $f_s$  and  $f_b$  in a local region are defined as:

$$\begin{cases} f_s = \text{mean}(I(y)|y \in \Omega_x \cap u(y) < 0.5) \\ f_b = \text{mean}(I(y)|y \in \Omega_x \cap u(y) > 0.5) \end{cases} \quad (11)$$

where  $u(y)$  is the fuzzy membership function in the local image domain  $\Omega_x$ . Here, a spatial weight  $\omega(x, y)$  is used to extract the local image information and defined as follows:

$$\omega(x, y) = \frac{1}{1 + |x - y|} \quad (12)$$

where  $\omega(x, y)$  is a  $(2k+1) \times (2k+1)$  square window. Therefore, two constants  $f_s$  and  $f_b$  can be rewritten as:

$$f_b = \frac{\int_{\Omega} \int_{\Omega_x} \omega(x, y) I(x) [u(x)]^m dy dx}{\int_{\Omega} \int_{\Omega_x} \omega(x, y) [u(x)]^m dy dx} \quad f_s = \frac{\int_{\Omega} \int_{\Omega_x} \omega(x, y) I(x) [1 - u(x)]^m dy dx}{\int_{\Omega} \int_{\Omega_x} \omega(x, y) [1 - u(x)]^m dy dx} \quad (13)$$

The region energy  $F^R$  is defined as follows:

$$F^R(u, g) = F^{HFR}(u, g) + F^{LFR}(u, g) \quad (14)$$

where  $F^{HFR}$  is the hybrid fuzzy region term,  $F^{LFR}$  is the local fuzzy region term, and  $g$  is an edge detector and defined as follows:

$$g(x) = \frac{1}{1 + |\nabla G_{\sigma} * I(x)|^2} \quad (15)$$

where  $\nabla G_{\sigma} * I(x)$  is the convolution of an image  $I(x)$  with standard deviation  $\sigma$ , whose purpose is to reduce the image noise and smooth the image edge.

By incorporating the local and global spatial region information into the FEAC model, the hybrid fuzzy region term  $F^{HFR}$  is given as follows:

$$F^{HFR}(u, g) = \lambda_1 \int_{\Omega} [u(x)]^m g(I(x) - (f_b + c_1)/2)^2 dx + \lambda_2 \int_{\Omega} [1 - u(x)]^m g(I(x) - (f_s + c_2)/2)^2 dx \quad (16)$$

where  $\lambda_1$  and  $\lambda_2$  are positive weighted parameters, and  $m$  is the weighting exponent on each fuzzy membership.

In the local fuzzy region term, we first define the energy functional by incorporating spatial and local information for pixel  $x$  in a local region:

$$\mathcal{E}^{loc}(x) = \alpha_1 \int_{in(C) \cap \Omega_x} \omega(x, y) (I(y) - f_b)^2 dy + \alpha_2 \int_{out(C) \cap \Omega_x} \omega(x, y) (I(y) - f_s)^2 dy \quad (17)$$

where  $\alpha_1$  and  $\alpha_2$  are two positive constants, which are used to balance the effects of the object and background region, and  $in(C)$  and  $out(C)$  denote the interior region and the exterior region along the curve  $C$ , respectively.

It can be seen that the value of the spatial constraint changes according to its distances from the central pixel  $x$  within the local window. With the fuzzy set defined in [24], the local fuzzy region term in the whole image domain  $\Omega$  is defined as follows:

$$\begin{aligned} F^{LFR}(u, g) &= \int_{\Omega} \mathcal{E}^{loc}(x) dx = \int_{\Omega} \left( \alpha_1 \int_{in(C) \cap \Omega_x} \omega(x, y) g(I(y) - f_b)^2 dy \right) dx + \int_{\Omega} \left( \alpha_2 \int_{out(C) \cap \Omega_x} \omega(x, y) g(I(y) - f_s)^2 dy \right) dx \\ &= \alpha_1 \int_{\Omega} [u(x)]^m \int_{\Omega} \omega(x, y) (I(y) - f_b)^2 g dy dx + \alpha_2 \int_{\Omega} [1 - u(x)]^m \int_{\Omega} \omega(x, y) g(I(y) - f_s)^2 dy dx \end{aligned} \quad (18)$$

Therefore, by combining Eq. (16) and Eq. (18), the region energy in Eq. (9) is rewritten as:

$$\begin{aligned} F^R(u) &= \lambda_1 \int_{\Omega} [u(x)]^m g(I(x) - (f_b + c_1)/2)^2 dx + \lambda_2 \int_{\Omega} [1 - u(x)]^m g(I(x) - (f_s + c_2)/2)^2 dx \\ &\quad + \alpha_1 \int_{\Omega} [u(x)]^m \int_{\Omega} \omega(x, y) g(I(y) - f_b)^2 dy dx + \alpha_2 \int_{\Omega} [1 - u(x)]^m \int_{\Omega} \omega(x, y) g(I(y) - f_s)^2 dy dx \end{aligned} \quad (19)$$

To compute the pseudo LSF  $u(x)$ , keeping the variables  $f_s$  and  $f_b$  fixed and calculating the minimization of the energy in Eq. (19) w.r.t.  $u$ , we have

$$\begin{aligned} \frac{\partial F^R(u)}{u} &= \lambda_1 m [u(x)]^{m-1} g(I(x) - (f_b + c_1)/2)^2 + m \lambda_2 [1 - u(x)]^{m-1} g(I(x) - (f_s + c_2)/2)^2 \\ &\quad + m \alpha_1 [u(x)]^{m-1} \int_{\Omega} \omega(x, y) g(I(y) - f_b)^2 dy + m \alpha_2 [1 - u(x)]^{m-1} \int_{\Omega} \omega(x, y) g(I(y) - f_s)^2 dy = 0 \end{aligned} \quad (20)$$

The membership function  $u(x)$  can be presented as

$$u(x) = \frac{1}{1 + \left( \frac{\lambda_1(I(x) - (f_b + c_1)/2)^2 + \alpha_1 \int_{\Omega} \omega(x,y)(I(y) - f_b)^2 dy}{\lambda_2(I(x) - (f_s + c_2)/2)^2 + \alpha_2 \int_{\Omega} \omega(x,y)(I(y) - f_s)^2 dy} \right)^{\frac{1}{m-1}}} \quad (21)$$

The degree of membership function  $u(x)$  is then updated according to the alteration of the region energy  $\Delta F$ .

### 3.2. Formulation of edge energy

To regularize the pseudo LSF and maintain the appearance of the shape smoothness during evolution, the edge energy  $F^E$  consists of a regularization term and a penalty term. The edge energy is defined as:

$$F^E(u) = \beta_1 L(u - 0.5) + \beta_2 P(u - 0.5) \quad (22)$$

where  $\beta_1$  and  $\beta_2$  are positive parameters, the first term is the length of evolving contour to ensure the smoothness of the pseudo LSF, which is called the regularization term. The second term called as penalty term is to keep the consistency between the signed distance function and the pseudo LSF, and we have:

$$L(u = 0.5) = \int_{\Omega} \delta(u - 0.5) |\nabla(u - 0.5)| dx \quad (23)$$

$$P(u = 0.5) = \frac{1}{2} \int_{\Omega} (1 - |\nabla(u - 0.5)|)^2 dx \quad (24)$$

where  $\nabla$  denotes the Hamilton operator and  $(\nabla\varphi)_{x,y} = \left(\frac{\partial\varphi}{\partial x}, \frac{\partial\varphi}{\partial y}\right)$  is the gradient of  $\varphi = u - 0.5$ .

### 3.3. Numerical approximation

In the process of computing the region energy, to solve the problem of the region energy defined in Eq. (19), the minimization of the energy function in the popular region-based ACMs is gradient descent optimizer based on the Euler-Lagrange equation. But it converges very slowly. Inspired by the FEAC model [24], we directly compute the difference between the new and old energy functions  $\Delta F^R = \hat{F}^R - F^R$  to update the pseudo LSF. We first transfer the energy functional defined in Eq. (19) from the continuous space to the discrete space. Then, to improve the computational rate, we directly calculate the difference between the new energy and the old one. If the value  $\Delta F^R$  is negative, the new one is replaced. Otherwise, the old value is unchanged. It is notable that the global minimal energy functional is easy to obtain in an iterative way when the energy functional defined in Eq. (17) is convex. Therefore, in this paper, we first prove the proposed energy functional is convex (Appendix A).

Let  $P \in I$  be a given point in the image domain  $\Omega$ , its corresponding intensity value and the degree of membership be  $I_0$  and  $u_0$ , respectively, and the old total energy functional be  $F$ . Correspondingly, for the same point  $P$ , the new degree of membership is  $u_n$ . Four constant  $c_1, c_2, f_s$ , and  $f_b$  become four new ones:  $\hat{c}_1, \hat{c}_2, \hat{f}_s$ , and  $\hat{f}_b$ , and the new total energy is  $\hat{F}$  when the degree of membership is changed into  $u_n$ . It is observed that the updated value  $\hat{u}(x)$  of the degree of membership for pixel  $P$  defined in Eq. (21)  $\Omega$  is  $u_n$  in the whole image domain during each iteration. Therefore, for the whole image domain  $x \in \Omega$ , the updated membership functions  $\hat{u}(x)$  can be presented as  $\hat{u}(x) = \sum u_n$  and  $1 - \hat{u}(x) = \sum [1 - u_n]$ . The process of computing the difference of the energy functional  $\Delta F^R = \hat{F}^R - F^R$  is presented in Appendix B. The change of the energy function is given as follows:

$$\begin{aligned} \Delta F^R &= \hat{F}^R - F^R = \left( \hat{F}_A^{HFR} + \hat{F}_B^{HFR} \right) + \left( \hat{F}_C^{LFR} + \hat{F}_D^{LFR} \right) - \left( F_A^{HFR} + F_B^{HFR} \right) - \left( F_C^{LFR} + F_D^{LFR} \right) \\ &= \left( \hat{F}_A^{HFR} - F_A^{HFR} \right) + \left( \hat{F}_B^{HFR} - F_B^{HFR} \right) + \left( \hat{F}_C^{LFR} - F_C^{LFR} \right) + \left( \hat{F}_D^{LFR} - F_D^{LFR} \right) \end{aligned} \quad (25)$$

where the formulations are defined as follows:

$$F_A^{HFR} = \lambda_1 \sum_{\Omega} [u(x)]^m g(I(x) - (f_b + c_1)/2)^2 \quad (26)$$

$$F_B^{HFR} = \lambda_2 \sum_{\Omega} [1 - u(x)]^m g(I(x) - (f_s + c_2)/2)^2 \quad (27)$$

$$F_C^{LFR} = \alpha_1 \sum_{\Omega} [u(x)]^m \left[ \sum_{\Omega} \omega(x,y) g(I(y) - f_b(x))^2 \right] \quad (28)$$

$$F_D^{LFR} = \alpha_2 \sum_{\Omega} [1 - u(x)]^m \left[ \sum_{\Omega} \omega(x,y) g(I(y) - f_s(x))^2 \right] \quad (29)$$

$$\hat{F}_A^{HFR} = \lambda_1 \sum_{\Omega} [\hat{u}(x)]^m g \left( I(x) - (\hat{f}_b + \hat{c}_1) / 2 \right)^2 \quad (30)$$

$$\hat{F}_B^{HFR} = \lambda_2 \sum_{\Omega} [1 - \hat{u}(x)]^m g \left( I(x) - (\hat{f}_s + \hat{c}_2) / 2 \right)^2 \quad (31)$$

$$\hat{F}_C^{LFR} = \alpha_1 \sum_{\Omega} [\hat{u}(x)]^m \left[ \sum_{\Omega} \omega(x, y) g \left( I(y) - \hat{f}_b(x) \right)^2 \right] \quad (32)$$

$$\hat{F}_D^{LFR} = \alpha_2 \sum_{\Omega} [1 - \hat{u}(x)]^m \left[ \sum_{\Omega} \omega(x, y) g \left( I(y) - \hat{f}_s(x) \right)^2 \right] \quad (33)$$

and eight constants are written as:

$$c_1 = \frac{\int_{\Omega} [u(x)]^m I(x) dx}{\int_{\Omega} [u(x)]^m dx}, \quad c_2 = \frac{\int_{\Omega} [1 - u(x)]^m I(x) dx}{\int_{\Omega} [1 - u(x)]^m dx} \quad (34)$$

$$f_b = \frac{\sum_{\Omega} \omega(x, y) * [I(x)[u(x)]^m]}{\sum_{\Omega} \omega(x, y) * [u(x)]^m}, \quad f_s = \frac{\sum_{\Omega} \omega(x, y) * [I(x)[1 - u(x)]^m]}{\sum_{\Omega} \omega(x, y) * [1 - u(x)]^m} \quad (35)$$

$$\hat{c}_1 = \frac{\sum_{\Omega} I(x) \cdot [\hat{u}(x)]^m}{\sum_{\Omega} [\hat{u}(x)]^m}, \quad \hat{c}_2 = \frac{\sum_{\Omega} I(x) \cdot [1 - \hat{u}(x)]^m}{\sum_{\Omega} [1 - \hat{u}(x)]^m} \quad (36)$$

$$\hat{f}_b = \frac{\sum_{\Omega} \omega(x, y) * (I(x)[\hat{u}(x)]^m)}{\sum_{\Omega} \omega(x, y) * [\hat{u}(x)]^m}, \quad \hat{f}_s = \frac{\sum_{\Omega} \omega(x, y) * (I(x)[1 - \hat{u}(x)]^m)}{\sum_{\Omega} \omega(x, y) * [1 - \hat{u}(x)]^m} \quad (37)$$

where  $u(x)$  is the degree of membership for pixel  $x$ ,  $I(x)$  is the input image,  $*$  is the convolution operation, and  $\omega(x, y)$  is a spatial weighting coefficient.

From the above computing process, it can be seen that we can compute the difference between the old and new energy functions to judge whether the pseudo LSF need to update or not. In the computing process, the pseudo LSF in the FEAC model [24] is updated according to the alterations of the pixel-by-pixel energy function during the curve evolution. Therefore, the FEAC model has very complicated reasoning process and needs amounts of computation. Unlike the FEAC model, we directly compute the change of two energy functions: the old energy functional before updating and the new energy function after updating.

In the process of computing the edge energy, we calculate the derivative of the energy functional in Eq. (22) w.r.t.  $u$ , which is written as:

$$\frac{\partial F^E}{\partial u} = \beta_1 \delta_e(u - 0.5) \operatorname{div} \left( \frac{\nabla(u - 0.5)}{|\nabla(u - 0.5)|} \right) + \beta_2 \left( \nabla^2(u - 0.5) - \operatorname{div} \left( \frac{\nabla(u - 0.5)}{|\nabla(u - 0.5)|} \right) \right) \quad (38)$$

where  $\delta_e(u) = H_e'(u) = \frac{1}{\pi} \frac{\varepsilon}{\varepsilon^2 + u^2}$  is a Dirac function defined in [12],  $\varepsilon$  is a positive constant,  $\operatorname{div}(\cdot)$  is the divergence operation, and  $\nabla^2$  is the Laplace operator.

### 3.4. Description of algorithm steps

The computational procedure of the proposed algorithm is described as follows:

1. Specify an input image, and initial parameters: weighting constants  $\lambda_1, \lambda_2, \alpha_1, \alpha_2, \beta_1$ , and  $\beta_2$ , the maximum number of iterations  $\text{IterNum}$ , the local window  $(2k+1) \times (2k+1)$ , and the edge detector matrix  $g$ .
2. Initialize pseudo LSF: set  $u_0(x) > 0.5$  for one part, and  $u_0(x) < 0.5$  for the other.
3. Compute the initial averages  $c_1, c_2, f_s$ , and  $f_b$  using Eq. (34) and Eq. (35), and calculate the region energy including four terms  $F_A^{HFR}, F_B^{HFR}, F_C^{LFR}$ , and  $F_D^{LFR}$ , defined in Eq. (26) – Eq.(29).
4. Update parameters: the degree of membership  $u_n(x)$  using Eq. (21), the new constants  $\hat{c}_1, \hat{c}_2, \hat{f}_s$ , and  $\hat{f}_b$  using Eq. (36) and Eq. (37), and calculate the region energy including four terms  $\hat{F}_A^{HFR}, \hat{F}_B^{HFR}, \hat{F}_C^{LFR}$ , and  $\hat{F}_D^{LFR}$  defined in Eqs. (30)–(33).
5. Compute the difference between the new and old energy  $\Delta F^R = \hat{F}^R - F^R$  using the following equation:

$$\begin{aligned} \Delta F^R &= \hat{F}^R - F^R = \left( \hat{F}_A^{HFR} + \hat{F}_B^{HFR} \right) + \left( \hat{F}_C^{LFR} + \hat{F}_D^{LFR} \right) - \left( F_A^{HFR} + F_B^{HFR} \right) - \left( F_C^{LFR} + F_D^{LFR} \right) \\ &= \left( \hat{F}_A^{HFR} - F_A^{HFR} \right) + \left( \hat{F}_B^{HFR} - F_B^{HFR} \right) + \left( \hat{F}_C^{LFR} - F_C^{LFR} \right) + \left( \hat{F}_D^{LFR} - F_D^{LFR} \right) \end{aligned} \quad (39)$$

If  $\Delta F^R < 0$ , replace  $u_0$  with  $u_n$ ; otherwise, keep the old value  $u_0$ .

6. Regularize and smooth the pseudo level set function using the edge energy defined in Eq. (38).
7. Repeat steps 3–6 till the iterations are finished.

#### 4. Experiments and results

To check the segmentation performance of the proposed model, we test the synthetic and real images by adding high noise. In our model, eight parameters need setting, i.e., weighting parameters  $\lambda_1, \lambda_2, \alpha_1, \alpha_2, \beta_1$ , and  $\beta_2$ , the maximum number of iterations  $IterNum$ , and the size of local weighting coefficient  $\omega(x, y)$  truncated by a  $(2k + 1) \times (2k + 1)$  window. In the following experiments, the pseudo LSF  $u(x)$  set to 0.7 and 0.3 in the inside and outside regions, respectively, the default parameters are set as follows:  $m = 2$ , the local weighting window  $k = 3$ , the maximal number of iteration  $IterNum = 100$ ,  $\beta_1 = 1$ , and  $\beta_2 = 1$ . The experiments are processed on a 3.2-GHz Intel 4-core PC computer with 3 GB of memory and use the Matlab programming language. The code is available at the website: <https://github.com/fangchj2002/HLFRA>.

##### 4.1. Experiment results on synthetic and real images

To validate the efficiency of the proposed model, we first test the synthetic images by adding different types of noises shown in Fig. 2. The parameters are set as follows:  $\lambda_1 = \lambda_2 = 1$  and  $\alpha_1 = \alpha_2 = 0.01$ . In Fig. 2, three images in the first column are from the clean images corrupted by Gaussian noise with the mean 0 and the variance 0.2, speckle noise with variance 1, and salt & pepper noise with the variance 0.3. To examine the feature image defined in Eq. (16), we construct the local fitting image  $I^{LF}$  =  $\omega(x, y) * I$  shown in the second column. The final positions of the evolving curves and the segmentation results are shown in the third and fourth columns, respectively. Four pseudo LSFs corresponding to three final evolution contours are shown in the last column. It can be seen that the proposed model can still extract three objects though the images are greatly corrupted with different types of noises.

Figs. 3 and 4 show the segmentation results on the medical and cell images. To better describe the evolving process of the curves, six intermediate results during 5, 10, 15, 20, 25, and 30 iterations are shown in Fig. 3(b)–(g), respectively. Fig. 3(h) depicts the final stopping boundaries. For color image, the average value of image intensity is written as  $I = (I_R + I_G + I_B)/3$ , where  $I_R, I_G$ , and  $I_B$  denote the pixel values corresponding to the RGB components, respectively. The segmentation results for color cell image are shown in Fig. 4. The local fitting image, the intermediate results after 2 iterations, and the final positions of the evolving curves are shown in Fig. 4(b)–(d), respectively. The final result is shown in Fig. 4(e). From these figures, it can be seen that the proposed model needs more iterations to reach steady state when the considered images contain more severe intensity inhomogeneity.

Fig. 5 shows the segmentation process of the cell image with severe intensity inhomogeneity. The parameters in the experiments are set as follows:  $\lambda_1 = \lambda_2 = 1$  and  $\alpha_1 = \alpha_2 = 0.1$ . Fig. 5(a) is the original image with initial contour. Fig. 5(b)–(d) depicts the local fitting image, the final stopping boundaries and segmentation results using the proposed model, respec-

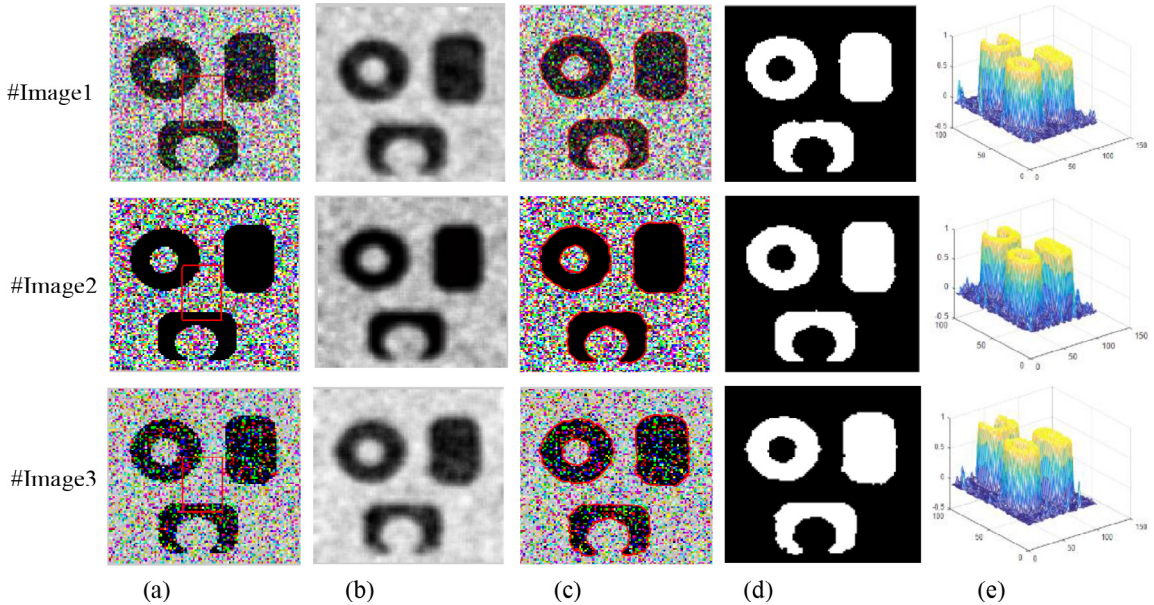


**Fig. 2.** Segmentation results of the proposed model on synthetic images. (a) Three images corrupted by different noise with initial contour; (b) The local fitting image; (c) The final positions of the stopping evolution curves; (d) The segmentation results of the proposed model; (e) 3D grid diagram of the final pseudo LSF ( $u-0.5$ ).

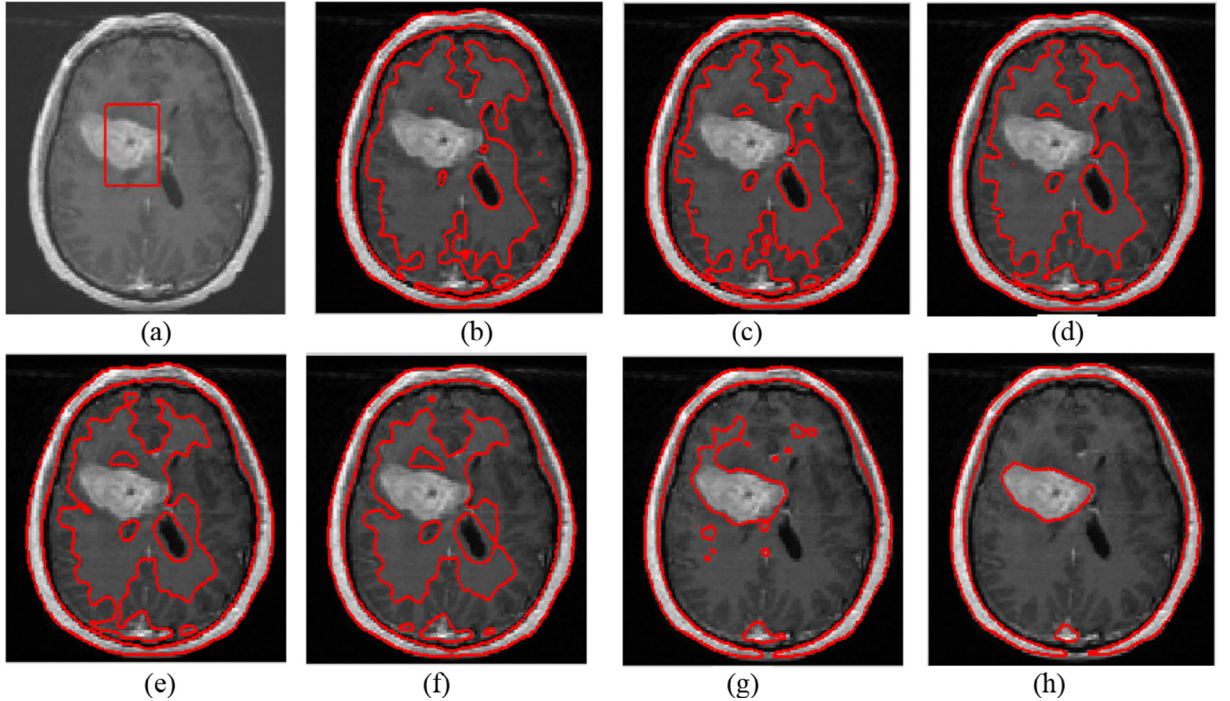


**Fig. 3.** Segmentation process for medical image with severe intensity inhomogeneity. (a) The original image with initial contour; (b–g) shows the intermediate positions of the evolution curves after 5, 10, 15, 20, 25 and 30 iterations; (h) shows the final position of evolution curve.

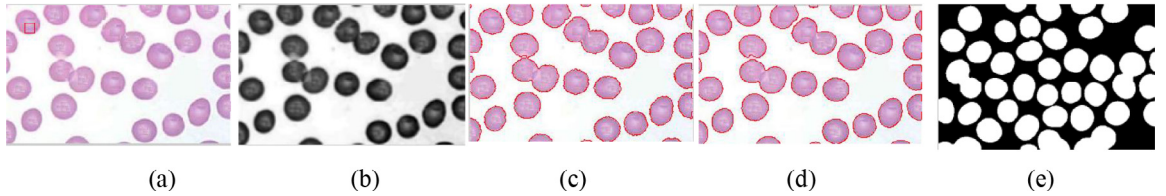


**Fig. 4.** (a) The color cell image with initial contour; (b) The fitting image; (c) The intermediate evolving process after 2 iterations; (d) The final positions of the evolution curves; (e) The segmentation result of the proposed model.

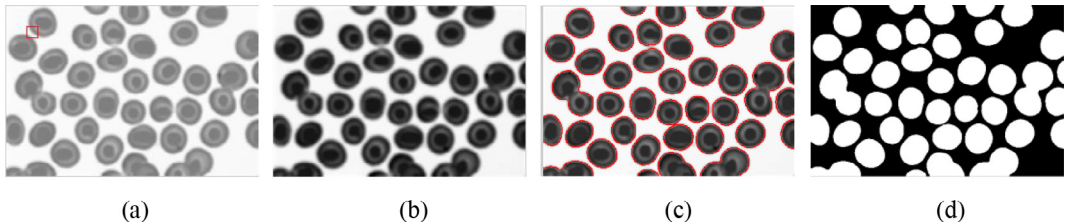


**Fig. 5.** Segmentation results of the proposed model on gray cell image. (a) The cell image with initial contour; (b) The fitting image; (c) The final positions of the evolution curves; (d) The segmentation results of the proposed model.

tively. The final pseudo LSF ( $\mathbf{u}=0.5$ ) is shown in Fig. 6(a). Fig. 6(b) shows the total energy (Blue line) and the changed energy  $\Delta F$  (Red line) during the curve evolution. The region energy including four terms  $\hat{F}_A^{HFR}$ ,  $\hat{F}_B^{HFR}$ ,  $\hat{F}_C^{LFR}$ , and  $\hat{F}_D^{LFR}$  in Eqs. (30)–(33) during 100 iterations is shown in Fig. 7(a), where four terms  $\hat{F}_A^{HFR}$ ,  $\hat{F}_B^{HFR}$ ,  $\hat{F}_C^{LFR}$ , and  $\hat{F}_D^{LFR}$  correspond with four lines marked with HFR-A, HFR-B, LFR-C, and LFR-D, respectively. The changes  $\Delta F_A^{HFR} = (\hat{F}_A^{HFR} - F_A^{HFR})$ ,  $\Delta F_B^{HFR} = (\hat{F}_B^{HFR} - F_B^{HFR})$ ,  $\Delta F_C^{LFR} = (\hat{F}_C^{LFR} - F_C^{LFR})$ , and  $\Delta F_D^{LFR} = (\hat{F}_D^{LFR} - F_D^{LFR})$  of four terms in the region energy are shown in Fig. 7(b). According to the segmentation results, it

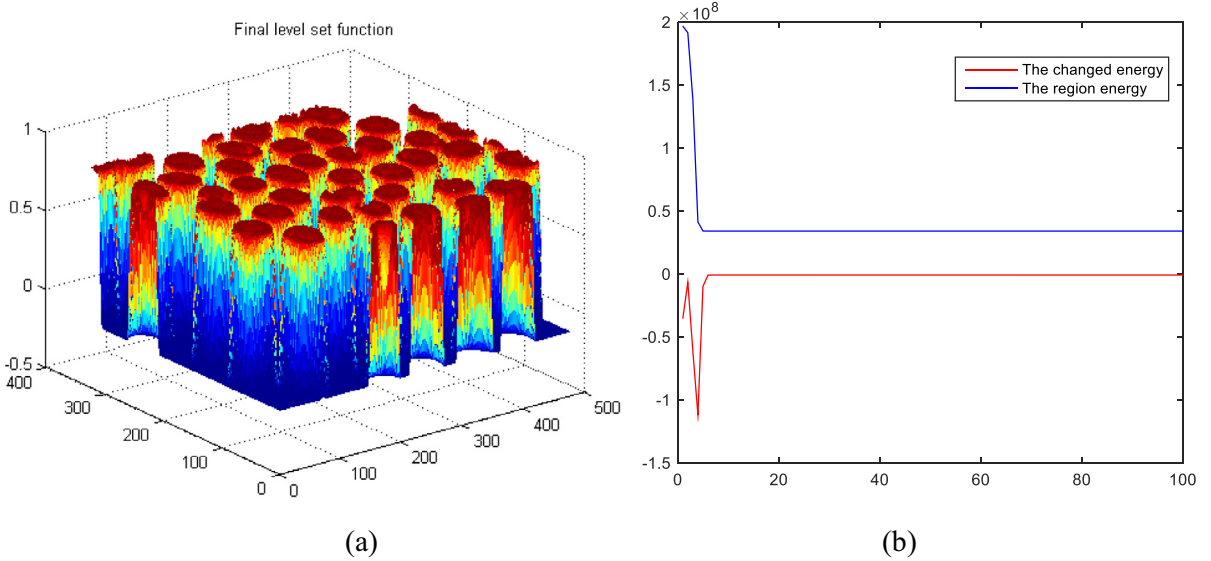


**Fig. 6.** (a) 3D grid diagram of the final pseudo LSF ( $u=0.5$ ); (b) The region energy (Blue Line) and the changed energy  $\Delta F$ (Red Line) correspond to the images in Fig. 5 during 100 iterations. (For interpretation of the references to color in this figure legend, the reader is referred to the web version of this article.)

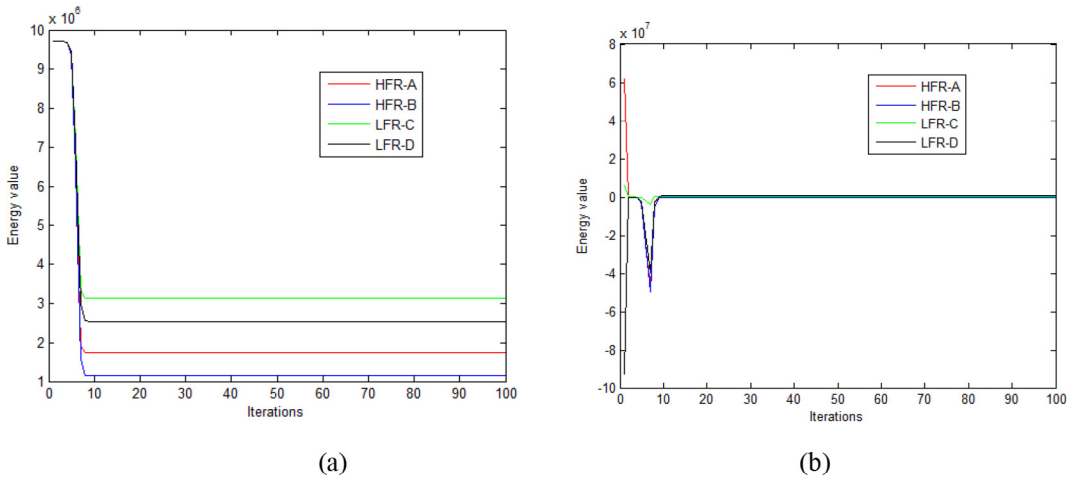


**Fig. 7.** The energy and the changed of four terms in the region energy defined in Eq. (19) corresponding to Fig. 5 during 100 iterations. (a) The energy of four terms  $\hat{F}_A^{HFR}$ ,  $\hat{F}_B^{HFR}$ ,  $\hat{F}_C^{LFR}$ , and  $\hat{F}_D^{LFR}$  in the region energy during curve evolution; (b) The changed energies  $\Delta F_A^{HFR}$ ,  $\Delta F_B^{HFR}$ ,  $\Delta F_C^{LFR}$ , and  $\Delta F_D^{LFR}$  during the curve evolution.

can be seen that the proposed model is able to accurately extract desired objects and can rapidly converge to the global optima in less than 10 iterations.

#### 4.2. Robustness to initialization

The following experiments validate the fuzziness of the energy, which provides a balanced technique with a strong ability to reject local minima. We test cell image with intensity inhomogeneity, and the segmentation results with different initial shapes are shown in Fig. 8. In the experiments, the parameters are set as follows:  $\lambda_1 = \lambda_2 = 1$  and  $\alpha_1 = \alpha_2 = 1$ . In the first row in Fig. 8(a)–(d), a cell image with different initial shapes is illustrated. The segmentation results are shown in the second row. To better illustrate the evolving process of the curves during 100 iterations, four region energies  $\hat{F}^R$  defined in Eq. (B-7) are shown in Fig. 9(a). Fig. 9(b) shows the changes  $\Delta F^R$  of the region energy in Eq. (25). It can be seen that the final contours with different initial shapes and positions are almost the same, and the proposed model reaches the steady state in less than 10 iterations.

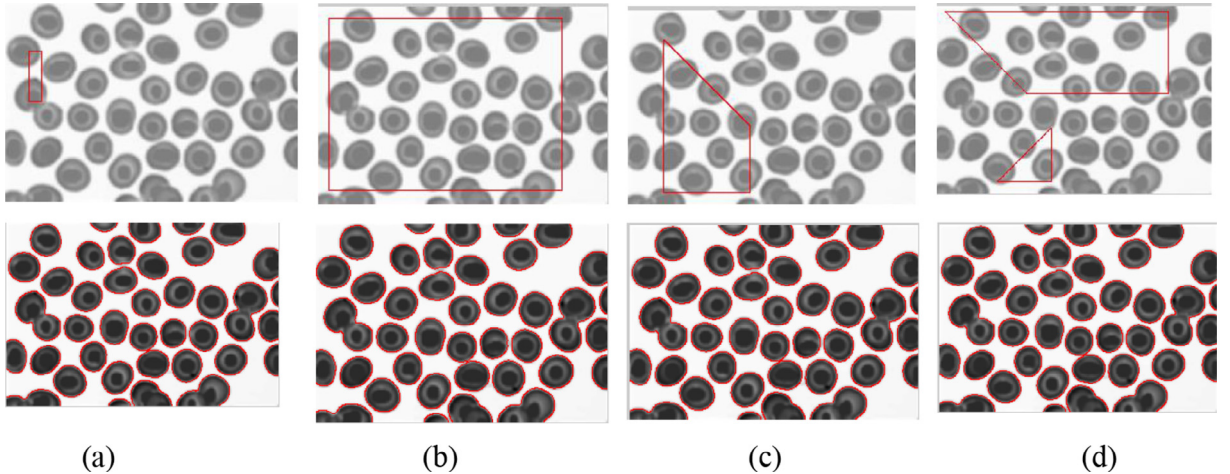


**Fig. 8.** Segmentation results for cell image with different shapes. In the first row: initial contours with different shapes; The second row: the final segmentation results.

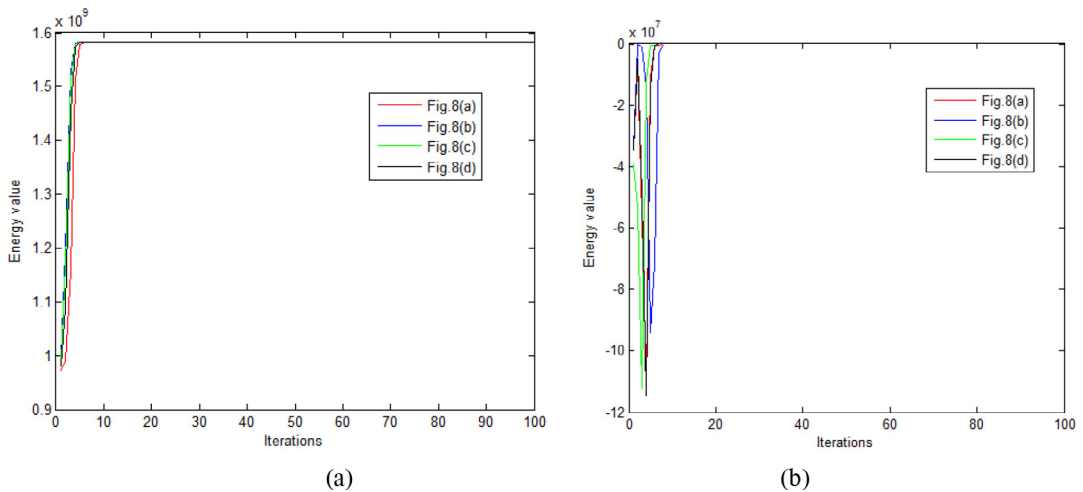


**Fig. 9.** The final region energy and the changed energy corresponding to the image in Fig. 8 during 100 iterations. (a) The final region energy  $\bar{F}^R$  during curve evolution; (b) The changed energy  $\Delta\bar{F}^R$  during curve evolution.

To further verify the proposed model independent on initial conditions, we tested another cell image with different initial shapes shown in Fig. 10. The parameters in the experiments are set as follows:  $\lambda_1 = 1.8$ ,  $\lambda_2 = 1$ , and  $\alpha_1 = \alpha_2 = 1$ . The different shapes with initial contour and the final stopping positions of the curves are shown in the first and second rows, respectively. The segmentation results show that the proposed model with different initial conditions (shapes and positions) can obtain the similar segmentation results. From these experiments, it can be seen that our model is robust to initialization.

#### 4.3. Comparison with the popular region-based ACMs

To demonstrate the performance of the proposed model, we compare the proposed model with the popular region-based ACMs, such as the Chan-Vese model [6], the LBF model [9], the LIF model [12], the FEAC model [24], the GL-FEAC model [25], the RGLFAC model [26], selective local or global segmentation (SLG) [30], the regularized level set models using fuzzy clustering (RLS-FC) [31], the local pre-fitting energy-based model (LPEM) [16], and the ACM with Hessian matrix (ACM-HM) [32]. The image feature determines accuracy of segmentation. It is known that one special segmentation method is not suitable for all kinds of images. Therefore, quantitative evaluation of these region-based ACMs is a necessary task. In this paper, we use average Dice coefficient [33] to measure performance with ground truth and region entropy [34,35] to measure performance without ground truth. Dice coefficient between two regions  $P$  and  $Q$  is defined as follows:

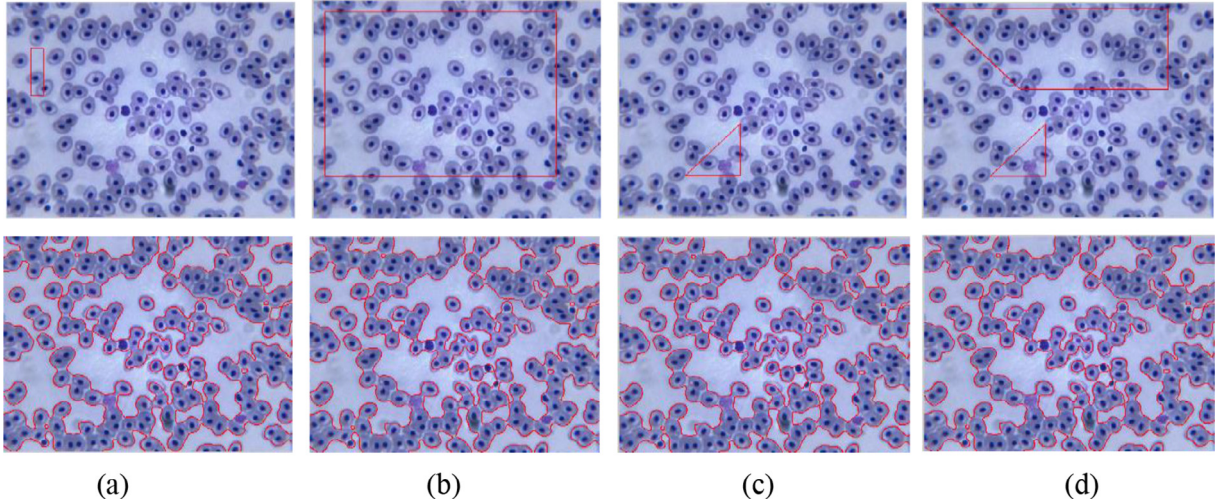


**Fig. 10.** Segmentation results for cell image with different shapes. In the first row: initial contours with different shapes; The second row: the final segmentation results.

$$J(P, Q) = \frac{2 \times |P \cap Q|}{|P| + |Q|} \quad (40)$$

where  $|P|$ ,  $|Q|$ , and  $|P \cap Q|$  are the pixel number of two regions  $P$ ,  $Q$ , and their union area, respectively. The closer the value  $J(P, Q)$  is to 1, the better the segmentation results is.

The region entropy is defined as:

$$RE = E_l(I) + E_r(I) \quad (41)$$

where  $E_l(I)$  and  $E_r(I)$  are a layout entropy and a desired region entropy, respectively. Here, they are defined as:

$$E_l(I) = - \sum_{i=1}^N \left( \frac{S_i}{S_I} \right) \log \left( \frac{S_i}{S_I} \right) \quad (42)$$

$$E_r(I) = - \sum_{i=1}^N \left( \frac{S_i}{S_I} \right) \sum_m \left( \frac{L_i(m)}{S_i} \right) \log \left( \frac{L_i(m)}{S_i} \right) \quad (43)$$

where  $S_i/S_I$  is the probability of a pixel belonging to region  $R_i$ , and  $L_i(m)$  is the number of pixels in region  $R_i$  which has value  $m$  of a luminance.

Figs. 11–14 depict the segmentation results for natural images with high intensity inhomogeneity using different region-based ACMs. The images are from the MSRA 10 K dataset [36] with their corresponding ground truth. To validate the robustness of the proposed model, high noise with the mean 0 and the variance 0.2 is added in these images. From these results in Figs. 11–14, it is noticeable that only the proposed model can exactly extract the objects in four images with high noise. The corresponding comparative results in terms of average Dice coefficient and average running time are shown in Tables 1 and 2. From these tables, it is also seen that the proposed model has the largest values in terms of average Dice coefficient in all of the region-based ACMs. Moreover, the proposed model takes the least running time because its convex region energy causes fast convergence.

To further validate the robustness of the proposed model, we test cell images shown in Figs. 15–18. The cell images in Figs. 15–18 are from the image in Fig. 10, the image in Fig. 4 corrupted by Gaussian noise, the image in Fig. 4 corrupted by speckle noise, and the image in Fig. 8 corrupted by Gaussian noise, respectively. Therefore, it is a challenging task to accurately extract the desired object boundaries in these images with severe intensity inhomogeneity. From these results, it is noted that only the proposed model can exactly extract the objects in four images. To clearly present the performance and efficiency, comparative results in terms of region entropy and average running time are shown in Tables 3 and 4. From these figures, it can be seen that the Chan-Vese and FEAC model mainly extract the brightest regions by the global energy, and the LIF, RLS-FC, and GL-FEAC models can obtain better results than in the LBF and SLG models for noisy images. Meanwhile, the ACM-HM can extract the region with maximum gradient boundaries, and the LPEM model gets the worst performance since it cannot dynamically update the local image information by computing average image intensities locally before the evolution of curve. From these tables, it is also seen that LBF model occupied the most running time of all the segmented images. On the other hand, the FEAC model takes the least average time while our model takes minimum executing time.

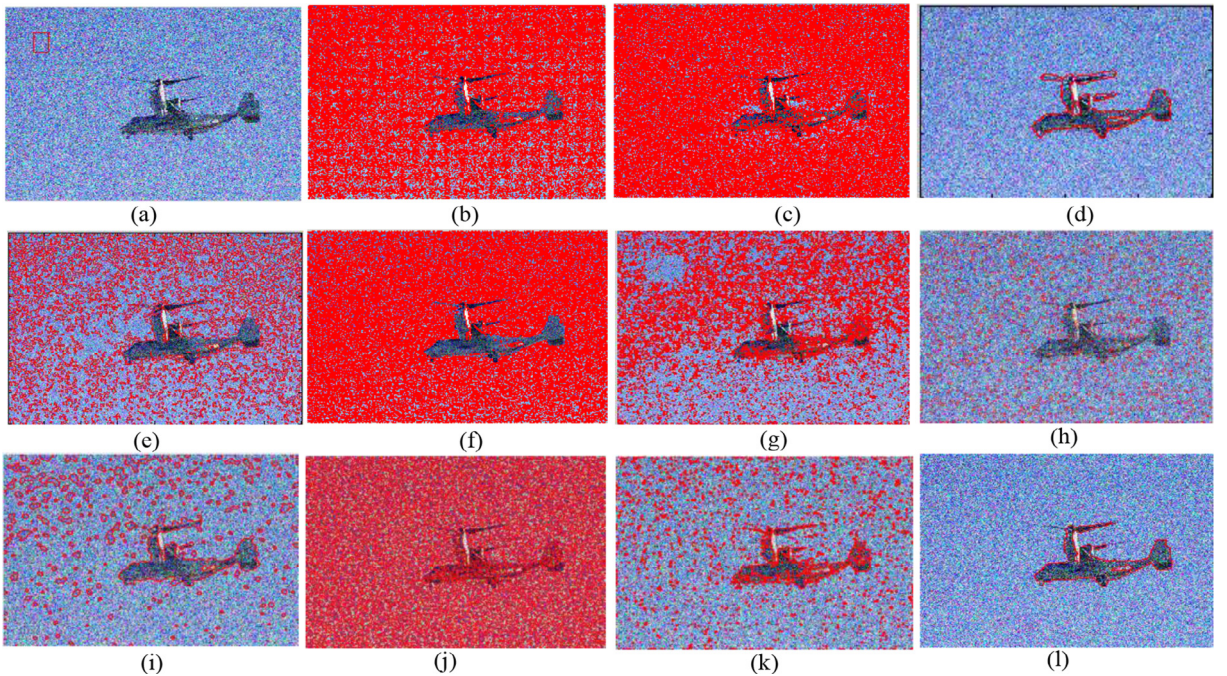


**Fig. 11.** Segmentation results for natural image corrupted by Gaussian noise using different models. (a) The original image with initial curve; (b) C-V; (c) LBF; (d) LIF; (e) SLG; (f) FEAC; (g) GL-FEAC; (h) RGLFAC; (i) RLS-FC; (j) LPEM; (k) ACM-HM; (l) The proposed model.

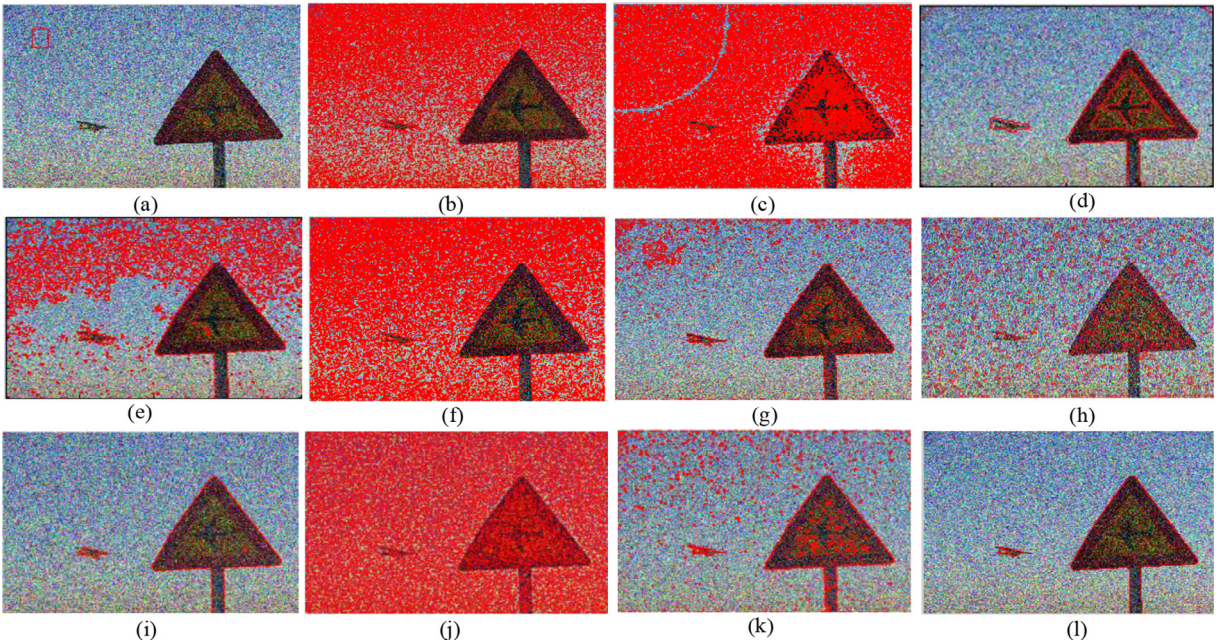


**Fig. 12.** Segmentation results for natural image corrupted by Gaussian noise using different models. (a) The original image with initial curve; (b) C-V; (c) LBF; (d) LIF; (e) SLG; (f) FEAC; (g) GL-FEAC; (h) RGLFAC; (i) RLS-FC; (j) LPEM; (k) ACM-HM; (l) The proposed model.

#### 4.4. Effect of parameters

To illustrate the effect of parameters, the segmentation results with different parameters on medical images with severe intensity inhomogeneity are shown in Figs. 19 and 20. In Fig. 19, the initial curve is shown in Fig. 19(a). In Fig. 19(b)–(d), we keep  $\alpha_1 = \alpha_2 = 0.1$  and  $\beta_1 = \beta_2 = 1$  fixed, and set weighting parameters  $\lambda_1$  and  $\lambda_2$  to  $(1.5, 1)$ ,  $(1, 1)$ , and  $(1, 1.5)$ , respec-

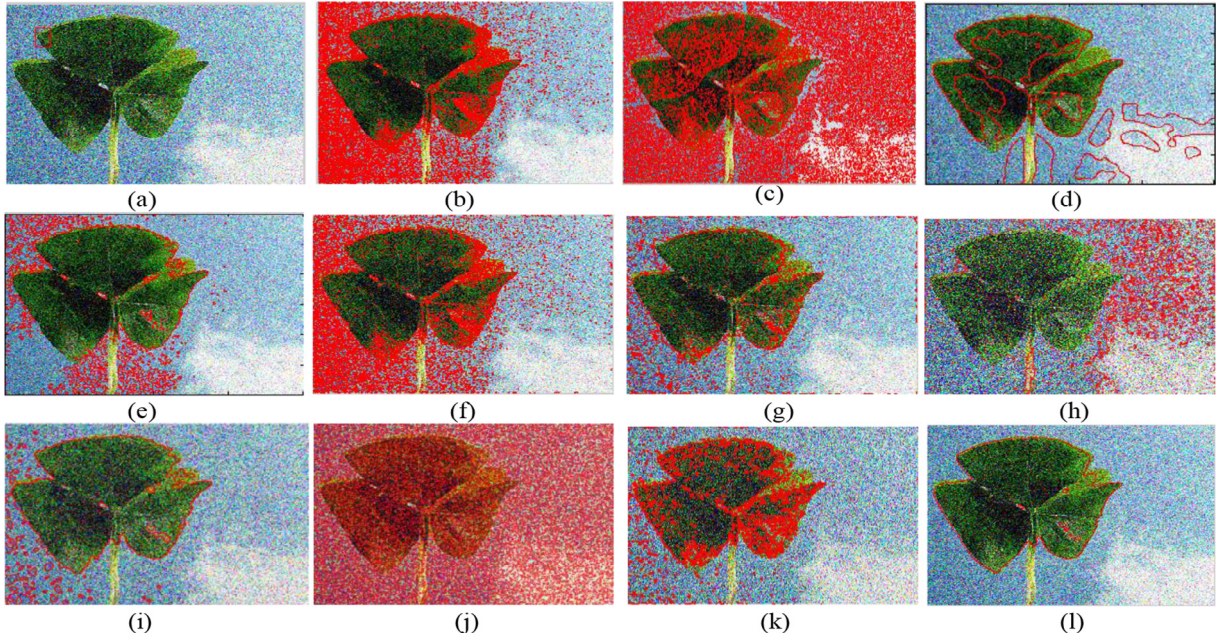


**Fig. 13.** Segmentation results for natural image corrupted by Gaussian noise using different models. (a) The original image with initial curve; (b) C-V; (c) LBF; (d) LIF; (e) SLG; (f) FEAC; (g) GL-FEAC; (h) RGLFAC; (i) RLS-FC; (j) LPEM; (k) ACM-HM; (l) The proposed model.

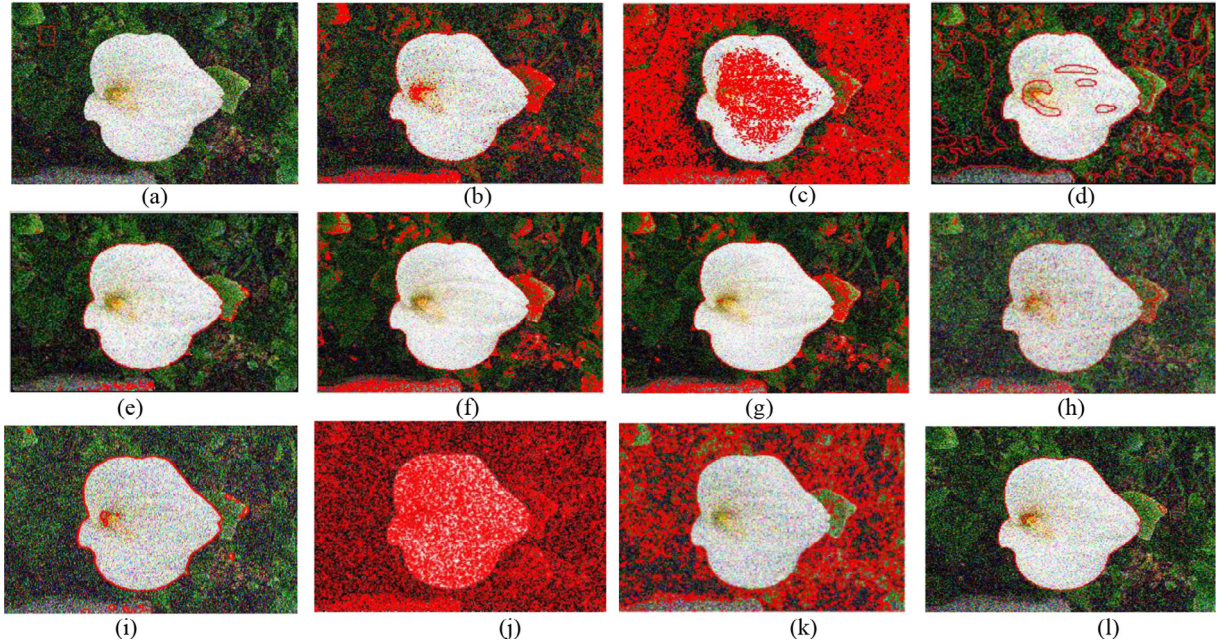


**Fig. 14.** Segmentation results for natural image corrupted by Gaussian noise using different models. (a) The original image with initial curve; (b) C-V; (c) LBF; (d) LIF; (e) SLG; (f) FEAC; (g) GL-FEAC; (h) RGLFAC; (i) RLS-FC; (j) LPEM; (k) ACM-HM; (l) The proposed model.

tively. Then, we keep the parameters  $\lambda_1$ ,  $\lambda_2$ ,  $\beta_1$ , and  $\beta_2$  fixed corresponding to Fig. 19(b)–(d), and change the weighting parameters of the local fuzzy term  $\alpha_1 = \alpha_2 = 0.5$ . The corresponding segmentation results are shown in Fig. 19(e)–(g). Finally, we verify the effect of edge region and set the weighting parameters  $\beta_1 = \beta_2 = 0$ . Its corresponding segmentation results are shown in Fig. 19(h). In Fig. 20, the initial curve is shown in Fig. 20(a). In Fig. 20(b)–(d), the parameters are kept  $\alpha_1 = \alpha_2 = 0.1$  and  $\beta_1 = \beta_2 = 1$  fixed, and the parameters  $\lambda_1$  and  $\lambda_2$  are set to (2, 1), (1, 1), and (0.1, 1). Then, we keep the parameters  $\lambda_1$ ,  $\lambda_2$ ,  $\beta_1$ , and  $\beta_2$  fixed, and set the weighting parameters  $\alpha_1 = \alpha_2 = 0.5$  in Fig. 20(e)–(g), respectively. In Fig. 20

**Table 1**

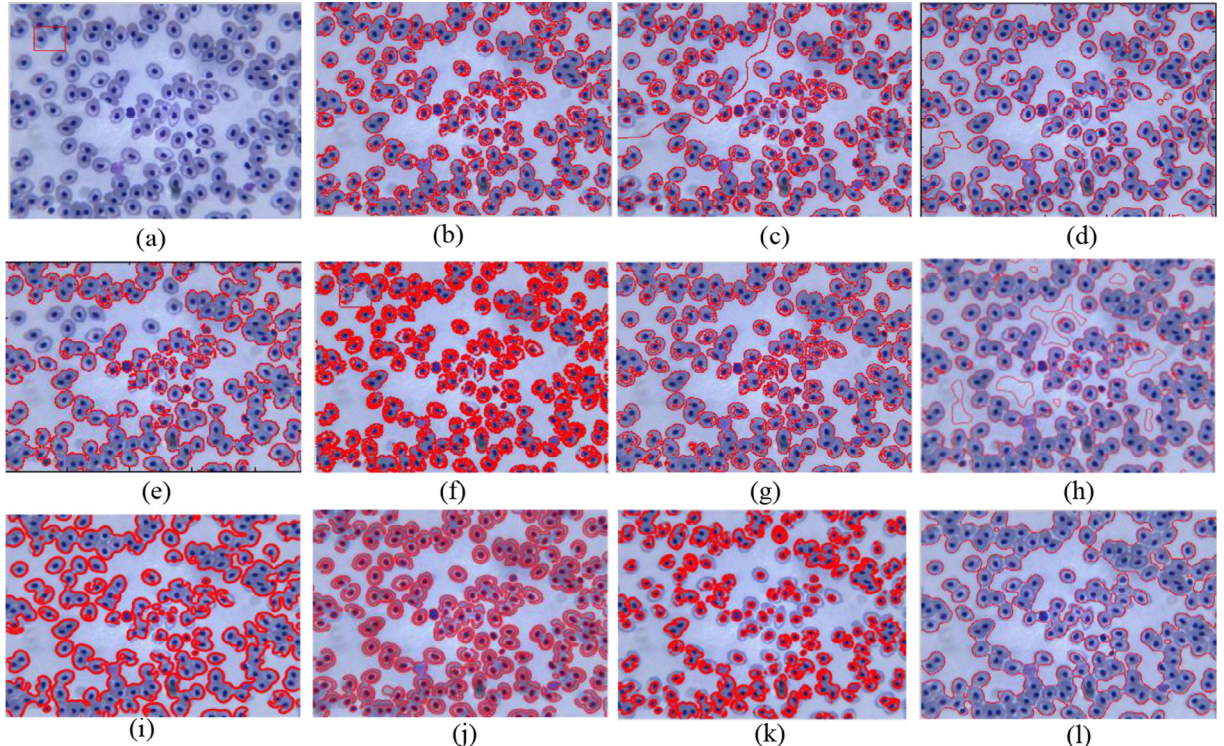
Comparison of the region-based ACMs in terms of average Dice coefficient.

Image	C-V	LBF	LIF	SLG	FEAC	GL-FEAC	RGLFAC	RLS-FC	LPEM	ACM-HM	Our
Image in Fig. 11	0.6353	0.4682	0.9407	0.7814	0.6014	0.7906	0.3284	0.7465	0.2846	0.7243	<b>0.9738</b>
Image in Fig. 12	0.6446	0.5149	0.8604	0.7104	0.6536	0.8548	0.3876	0.9018	0.3146	0.7569	<b>0.9787</b>
Image in Fig. 13	0.7014	0.5871	0.8418	0.7248	0.8347	0.8827	0.3174	0.8341	0.2867	0.7195	<b>0.9674</b>
Image in Fig. 14	0.7896	0.6549	0.7403	0.9123	0.8469	0.8684	0.8149	0.9146	0.3582	0.6873	<b>0.9584</b>

**Table 2**

Comparison of the region-based ACMs in terms of running time and iterations.

Segmentation model	Image in Fig. 11		Image in Fig. 12		Image in Fig. 13		Image in Fig. 14	
	Time	Iterations	Time	Iterations	Time	Iterations	Time	Iterations
C-V	45.625	145	213.434	730	51.684	500	96.0657	1000
LBF	61.064	220	66.419	220	72.273	220	72.409	220
LIF	69.897	450	69.967	450	67.115	450	112.713	450
SLG	102.687	200	76.107	200	37.256	200	7.062	200
FEAC	9.466	100	9.968	100	10.052	100	9.873	100
GL-FEAC	12.086	100	12.412	100	11.152	100	11.598	100
RGLFAC	11.466	100	11.657	100	11.594	100	10.957	100
RLS-FC	7.753	100	8.149	100	8.245	100	7.864	100
LPEM	25.635	900	24.096	900	23.236	900	23.206	900
ACM-HM	9.018	50	9.284	50	9.546	50	8.418	50
<b>Our</b>	<b>3.744</b>	<b>40</b>	<b>3.981</b>	<b>40</b>	<b>3.535</b>	<b>40</b>	<b>3.729</b>	<b>40</b>

**Fig. 15.** Segmentation results for cell image using different models. (a) The original image with initial curve; (b) C-V; (c) LBF; (d) LIF; (e) SLG; (f) FEAC; (g) GL-FEAC; (h) RGLFAC; (i) RLS-FC; (j) LPEM; (k) ACM-HM; (l) The proposed model.

(h), the edge energy is removed ( $\beta_1 = \beta_2 = 0$ ). It can be seen that the proposed model can obtain satisfactory result when  $\lambda_1$  is greater than  $\lambda_2$  by keeping  $\beta_1 = \beta_2 = 1$  in Fig. 20(a) because the object region is brighter than the background region.

From two sets of experimental results, it can be seen that the model can handle higher intensity inhomogeneity when we reduce the weighting values  $\alpha_1$  and  $\alpha_2$ . The segmentation results contains more noise when the edge energy is removed ( $\beta_1 = \beta_2 = 0$ ). If the region inside the contour is brighter than the region outside the contour, the selected value  $\lambda_1$  is larger

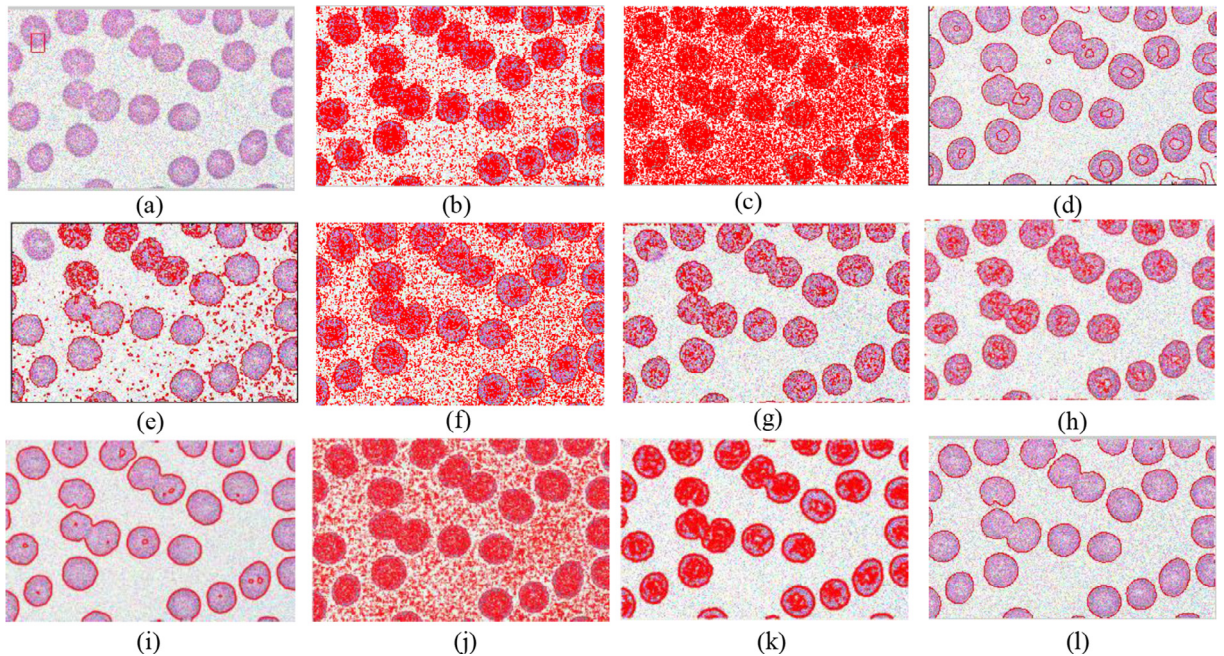


**Fig. 16.** Segmentation results for cell image corrupted by Gaussian noise using different models. (a) The original image with initial curve; (b) C-V; (c) LBF; (d) LIF; (e) SLG; (f) FEAC; (g) GL-FEAC; (h) RGLFAC; (i) RLS-FC; (j) LPEM; (k) ACM-HM; (l) The proposed model.

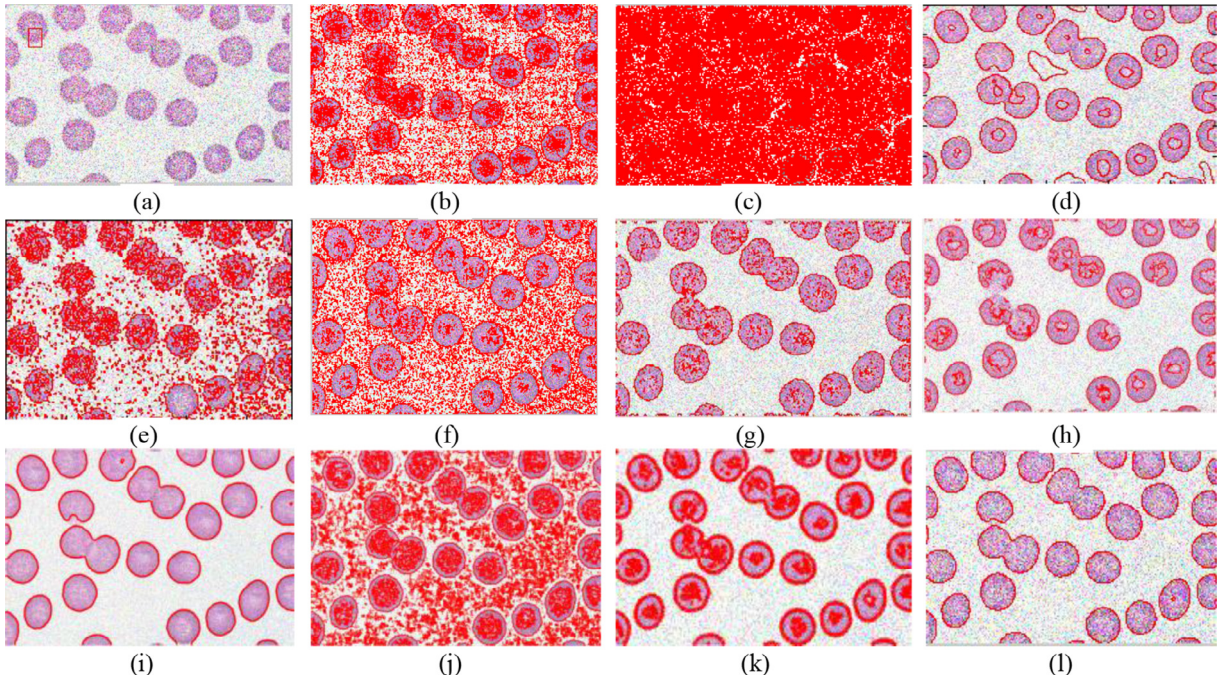


**Fig. 17.** Segmentation results for cell image corrupted by speckle noise using different models. (a) The original image with initial curve; (b) C-V; (c) LBF; (d) LIF; (e) SLG; (f) FEAC; (g) GL-FEAC; (h) RGLFAC; (i) RLS-FC; (j) LPEM; (k) ACM-HM; (l) The proposed model.

than the value  $\lambda_2$ . Otherwise, the selected value  $\lambda_1$  is smaller than the value  $\lambda_2$ . Similarly, the weights  $\alpha_1$  and  $\alpha_2$  of the fitting terms in Eq. (19) is to control the degree of intensity inhomogeneity in given images. If the given image contains severe intensity inhomogeneity, a small value should be chosen, and vice versa.

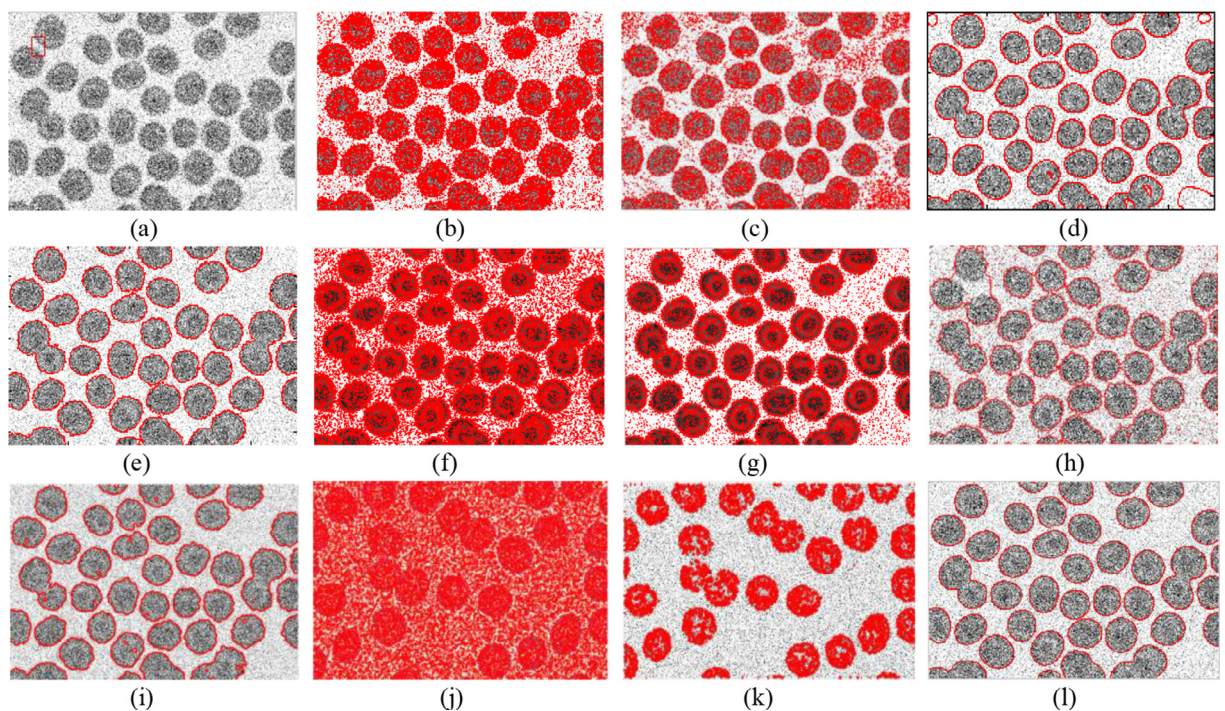


**Fig. 18.** Segmentation results for cell image corrupted by Gaussian noise using different models. (a) The original image with initial curve; (b) C-V; (c) LBF; (d) LIF; (e) SLG; (f) FEAC; (g) GL-FEAC; (h) RGLFAC; (i) RLS-FC; (j) LPEM; (k) ACM-HM; (l) The proposed model.

**Table 3**

Comparison of the region-based ACMs in terms of region entropy.

Image	C-V	LBF	LIF	SLG	FEAC	GL-FEAC	RGLFAC	RLS-FC	LPEM	ACM-HM	Our
Image in Fig. 15	4.896	4.754	4.418	5.154	4.796	4.847	5.274	5.049	5.572	4.986	<b>4.315</b>
Image in Fig. 16	5.314	5.641	4.648	4.813	5.461	4.462	4.864	4.427	5.767	4.953	<b>4.207</b>
Image in Fig. 17	5.242	5.867	4.829	4.995	5.583	4.682	4.765	4.308	5.867	4.806	<b>4.286</b>
Image in Fig. 18	5.624	5.567	4.606	4.466	5.791	5.162	4.784	4.382	6.218	5.076	<b>4.254</b>

**Table 4**

Comparison of the region-based ACMs in terms of average running time and iterations.

Segmentation model	Image in Fig. 15		Image in Fig. 16		Image in Fig. 17		Image in Fig. 18	
	Time	Iterations	Time	Iterations	Time	Iterations	Time	Iterations
Chan-Vese	14.533	180	35.429	130	49.591	140	50.192	150
LBF	40.563	220	113.256	220	114.559	220	86.390	220
LIF	93.308	450	86.621	450	101.521	450	85.597	450
SLG	7.607	200	46.615	200	143.181	200	21.994	200
FEAC	10.453	100	9.174	100	8.732	100	9.576	100
GL-FEAC	13.081	100	12.275	100	11.572	100	12.672	100
RGLFAC	22.412	100	18.377	100	16.634	100	23.825	100
RLS-FC	10.374	100	7.125	100	7.608	100	7.197	100
LPEM	51.611	900	39.327	900	40.343	900	40.374	900
ACM-HM	22.783	50	18.988	50	14.559	50	22.602	50
<b>Our</b>	<b>6.355</b>	<b>40</b>	<b>4.955</b>	<b>40</b>	<b>5.024</b>	<b>40</b>	<b>5.352</b>	<b>40</b>

## 5. Conclusion

In this paper, we present a novel hybrid and local fuzzy region-edge based active contour model to segment the images with high noise and intensity inhomogeneity. The HLFRA model includes two parts, namely, region energy and edge energy. In the first part, the region energy proved to be strictly convex consists of hybrid fuzzy region term and local fuzzy region term by incorporating different types of image features, and it can guide the evolving curves to move toward the object. In

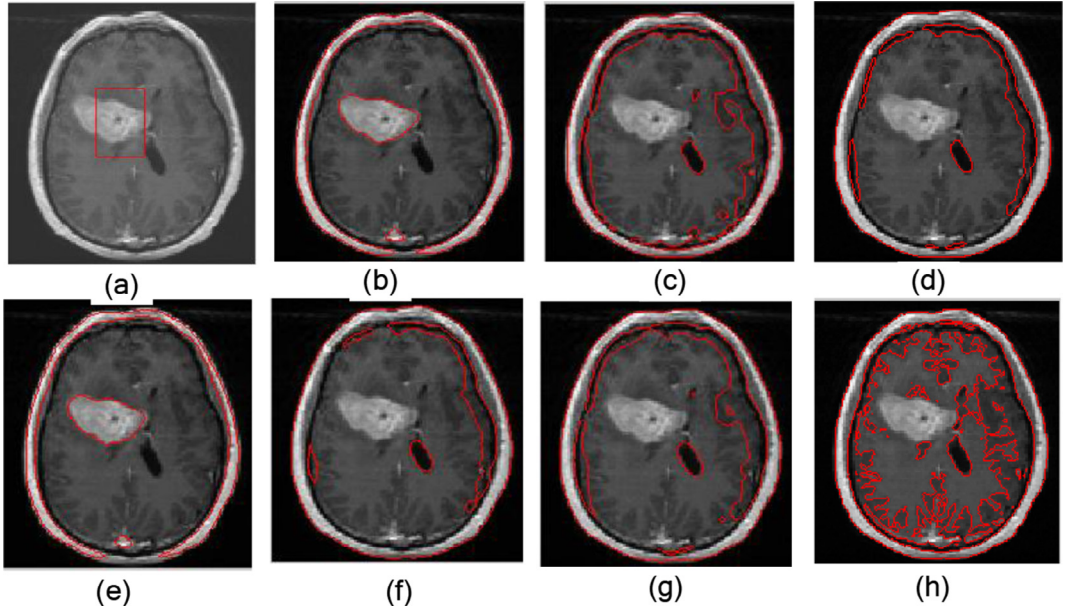


**Fig. 19.** The segmentation results of the proposed model with different parameters for medical image. (a) The original image with initial contour; (b-d) Keeping  $\alpha_1 = \alpha_2 = 0.1$  and  $\beta_1 = \beta_2 = 1$  fixed, the parameters  $\lambda_1$  and  $\lambda_2$  are set to  $(1.5, 1)$ ,  $(1, 1)$ , and  $(1, 1.5)$ , respectively; (e-g) Keeping  $\alpha_1 = \alpha_2 = 0.5$  and  $\beta_1 = \beta_2 = 1$  fixed, the parameters  $\lambda_1$  and  $\lambda_2$  are set to  $(1.5, 1)$ ,  $(1, 1)$ , and  $(1, 1.5)$ , respectively; (h) Parameter setting:  $\lambda_1 = 1.5$ ,  $\lambda_2 = 1$ ,  $\alpha_1 = \alpha_2 = 0.1$ , and  $\beta_1 = \beta_2 = 0$ .

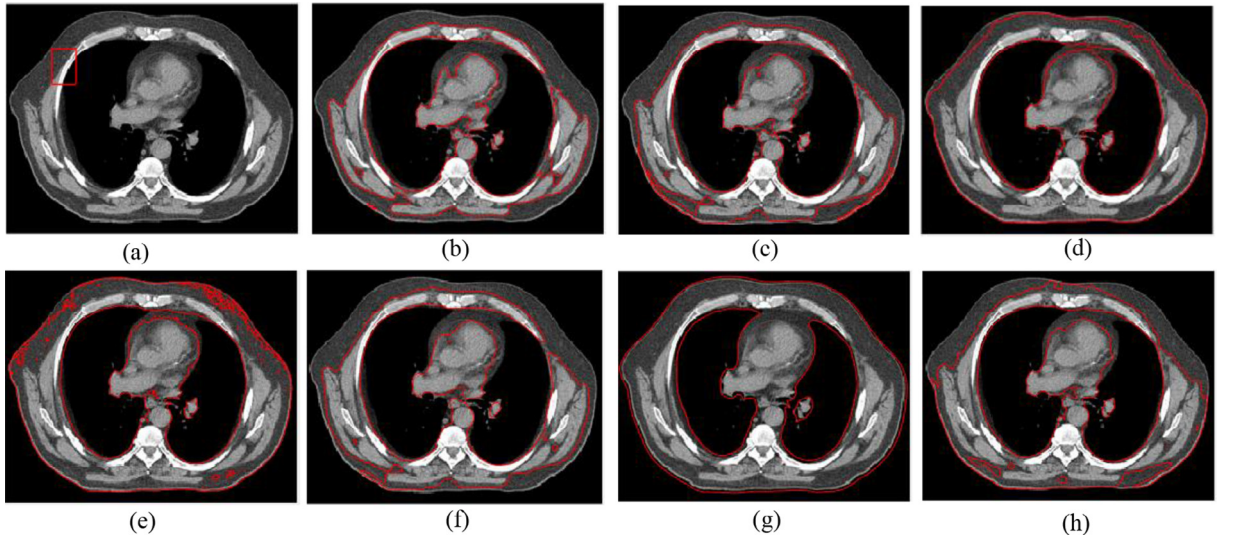


**Fig. 20.** The segmentation results of the proposed model with different parameters. (a) The original image with initial contour; (b-d) Keeping  $\alpha_1 = \alpha_2 = 0.1$  and  $\beta_1 = \beta_2 = 1$  fixed, the parameters  $\lambda_1$  and  $\lambda_2$  are set to  $(2, 1)$ ,  $(1, 1)$ , and  $(0.1, 1)$ , respectively; (e-g) Keeping  $\alpha_1 = \alpha_2 = 0.5$  and  $\beta_1 = \beta_2 = 0.5$  fixed, the parameters  $\lambda_1$  and  $\lambda_2$  are set to  $(2, 1)$ ,  $(1, 1)$ , and  $(0.1, 1)$ , respectively; (h) Parameter setting:  $\lambda_1 = 0.1$ ,  $\lambda_2 = 1$ ,  $\alpha_1 = \alpha_2 = 0.1$ , and  $\beta_1 = \beta_2 = 0$ .

the second part, the edge energy can make the evolving curve accurately stop on the object boundaries. In addition, a simpler method by computing the difference between the new and old energy functions is developed to update the pseudo LSF. The experimental results show that the proposed model can successfully extract the object from both synthetic and real images with high noise and intensity inhomogeneity. Moreover, it is experimentally verified that the convex region energy ensures the segmentation results independent of initial conditions (positions and shapes). In future, our model can be applied to many famous ACMs, such as kernel space [37] and multi-phase image segmentation [12].

## CRediT authorship contribution statement

**Jiangxiong Fang:** Conceptualization, Methodology, Software, Writing - original draft. **Huaxiang Liu:** Software, Writing - original draft. **Liting Zhang:** Writing - review & editing. **Jun Liu:** Writing - review & editing. **Hesheng Liu:** Supervision, Writing - review & editing.

## Declaration of Competing Interest

The authors declare that they have no known competing financial interests or personal relationships that could have appeared to influence the work reported in this paper.

## Acknowledgments

The work was supported by the National Natural Science Foundation of China (No. 61866001, No. 61966001, No. 61463005, No. 21664002, and No. 61463017), China Postdoctoral Science Foundation (No. 2017 M612163), Natural Science Foundation of Jiangxi Province (No. 20192BAB207028, No. 20181BAB211017 and No. 20171BAB202028), Jiangxi Provincial Key Laboratory of Digital Land (DLJ201804), Science and technology project of Jiangxi Provincial Department of Education (No. GJJ170450, and No.GJJ160539).

## Appendix A. The proof of convexity for region energy

The region energy function of the proposed model in Eq. (19) can be written as follows:

$$F^R(u) = \lambda_1 F_A^{HFR}(u, g) + \lambda_2 F_B^{HFR}(u, g) + \alpha_1 F_C^{LFR}(u, g) + \alpha_2 F_D^{LFR}(u, g), \quad u \in [0, 1] \quad (A1)$$

where  $F_A^{HFR}(u, g)$ ,  $F_B^{HFR}(u, g)$ ,  $F_C^{LFR}(u, g)$ , and  $F_D^{LFR}(u, g)$  are defined as:

$$F_A^{HFR}(u, g) = \int_{\Omega} [u(x)]^m g(I(x) - (f_b + c_1)/2)^2 dx \quad (A2)$$

$$F_B^{HFR}(u, g) = \int_{\Omega} (1 - [u(x)])^m g(I(x) - (f_s + c_1)/2)^2 dx \quad (A3)$$

$$F_C^{LFR}(u, g) = \int_{\Omega} [u(x)]^m \int_{\Omega} \omega(x, y) g|I(y) - f_b(x)|^2 dy \quad (A4)$$

and

$$F_D^{LFR}(u, g) = \int_{\Omega} [1 - u(x)]^m \int_{\Omega} \omega(x, y) g|I(y) - f_s(x)|^2 dy \quad (A5)$$

The equation  $F_A^{HFR}(u, g)$  in Eq. (A2) can be written as

$$\varepsilon_A^{HFR}(x, g) = [u(x)]^m g(I(x) - (f_b + c_1)/2)^2 \quad (A6)$$

and  $F_A^{SFR}(u, g) = \int_{\Omega} \varepsilon_A^{SFR}(x, g) dx$ .

Now we first prove the equation  $\varepsilon_A^{HFR}(x, g)$  is convex. Let  $x_1, x_2 \in \Omega$ , for  $\forall \theta \in [0, 1]$ . Then we have

$$\theta x_1 + (1 - \theta)x_2 = \theta(x_1 - x_2) + x_2 \in \Omega \quad (A7)$$

Therefore, the domain of  $\varepsilon_A^{HFR}(x, g)$  is convex. The second order derivative of Eq. (A6) w. r. t.  $u$ , and we have

$$\begin{aligned} \frac{\partial^2 \varepsilon_A^{HFR}}{\partial u^2} &= \frac{\partial}{\partial u} \left( \frac{\partial \varepsilon_A^{HFR}}{\partial u} \right) = \frac{\partial}{\partial u} \left( m[u(x)]^{m-1} g(I(x) - (f_b + c_1)/2)^2 \right) \\ &= m(m-1)[u(x)]^{m-2} g(I(x) - (f_b + c_1)/2)^2 \end{aligned} \quad (A8)$$

Since  $m > 1$ ,  $u(x) \in [0, 1]$ , and  $g(I(x) - (f_b + c_1)/2)^2 \geq 0$ , so  $\frac{\partial^2 \varepsilon_A^{HFR}}{\partial u^2} \geq 0$ .

Since the domain of  $\varepsilon_A^{HFR}(x, g)$  is convex and  $\frac{\partial^2 \varepsilon_A^{HFR}}{\partial u^2} \geq 0$ , so  $\varepsilon_A^{HFR}(x, g)$  is convex. Therefore,  $\forall x_1, x_2 \in \Omega$  and  $\theta \in [0, 1]$ , and we can get the following relation:

$$\varepsilon_A^{HFR}(\theta x_1 + (1 - \theta)x_2) \leq \theta \varepsilon_A^{HFR}(x_1) + (1 - \theta) \varepsilon_A^{HFR}(x_2) \quad (A9)$$

Calculating integral of the two sides of Eq. (A9), we obtain the following formulation:

$$\int_{\Omega} \varepsilon_A^{HFR}(\theta x_1 + (1 - \theta)x_2) dx \leq \theta \int_{\Omega} \varepsilon_A^{HFR}(x_1) dx + (1 - \theta) \int_{\Omega} \varepsilon_A^{HFR}(x_2) dx \quad (A10)$$

With  $F_A^{HFR}(u, g) = \int_{\Omega} \varepsilon_A^{HFR}(x, g) dx$ , Eq. (A10) can be rewritten as:

$$F_A^{HFR}(\theta x_1 + (1 - \theta)x_2) \leq \theta F_A^{HFR}(x_1) + (1 - \theta)F_A^{HFR}(x_2) \quad (\text{A11})$$

Hence,  $\varepsilon_A^{HFR}$  is convex.

Similarly, let

$$\varepsilon_B^{HFR}(x) = [1 - u(x)]^m g(I(x) - (f_s + c_2)/2)^2 \quad (\text{A12})$$

where  $\varepsilon_B^{HFR} : \Omega \rightarrow R$ . The equation (A2) is  $F_B^{HFR}(u, g) = \int_{\Omega} \varepsilon_B^{HFR}(x, g) dx$ . In the same way, we can also prove  $F_B^{HFR}(u, g)$  is convex.

The formulation  $F_C^{LFR}(u, g)$  in (A4) can be represented as follows:

$$F_C^{LFR}(u, g) = \int_{\Omega} \varepsilon_C^{LFR}(x) dx \quad (\text{A13})$$

and

$$\varepsilon_C^{LFR}(x) = [u(x)]^m \varepsilon_C^{LFR}(y) \quad (\text{A14})$$

$$\varepsilon_C^{LFR}(y) = \int_{\Omega} \omega(x, y) g|I(y) - f_b(x)|^2 dy \quad x, y \in R^2 \quad (\text{A15})$$

The second order derivative of Eq. (A14) w.r.t.  $u$  can be computed as follows:

$$\begin{aligned} \frac{\partial^2 \varepsilon_C^{LFR}(x)}{\partial u^2} &= \frac{\partial}{\partial u} \left( \frac{\partial \varepsilon_C^{LFR}(x)}{\partial u} \right) = \frac{\partial}{\partial u} \left( m[u(x)]^{m-1} \varepsilon_C^{LFR}(y) \right) \\ &= m(m-1)[u(x)]^{m-2} \varepsilon_C^{LFR}(y) \end{aligned} \quad (\text{A16})$$

Since  $m > 1$  and  $\varepsilon_C^{LFR}(y) \geq 0$ , so  $\frac{\partial^2 \varepsilon_C^{LFR}(x)}{\partial u^2} \geq 0$ .

Now  $\varepsilon_C^{LFR}(y)$  is convex because  $\varepsilon_C^{LFR}(x)$  is convex domain and  $\frac{\partial^2 \varepsilon_C^{LFR}(x)}{\partial u^2} \geq 0$ . Hence  $\forall x_1, x_2 \in \Omega$ , and  $\theta \in [0, 1]$ , we have

$$\varepsilon_C^{LFR}(\theta x_1 + (1 - \theta)x_2) \leq \theta \varepsilon_C^{LFR}(x_1) + (1 - \theta) \varepsilon_C^{LFR}(x_2) \quad (\text{A17})$$

Then, we integrate both sides of the above formula in (A17), and have

$$\int_{\Omega} \varepsilon_C^{LFR}(\theta x_1 + (1 - \theta)x_2) dx \leq \theta \int_{\Omega} \varepsilon_C^{LFR}(x_1) dx + (1 - \theta) \int_{\Omega} \varepsilon_C^{LFR}(x_2) dx \quad (\text{A18})$$

Therefore  $F_C^{LFR}(u, g) = \int_{\Omega} \varepsilon_C^{LFR}(x) dx = \int_{\Omega} [u(x)]^m \varepsilon_C^{LFR}(y) dx$  is also convex. In the same way, we can prove  $F_D^{LFR}(u, g)$  is convex.

In Eq. (A1), since  $\lambda_1 > 0$ ,  $\lambda_2 > 0$ ,  $\alpha_1 > 0$ , and  $\alpha_2 > 0$ , then the region energy  $F^R(u)$  consists of four weighting convex functionals. So the energy function  $F^R(u)$  is convex with regard to  $u$ .

## Appendix B. The process of the region energy

Two constants  $c_1$  and  $c_2$  in Eq. (7) can be written as:

$$c_1 = \frac{\sum_{\Omega} [I(x) \cdot [u(x)]^m]}{\sum_{\Omega} [u(x)]^m}, \text{ and } c_2 = \frac{\sum_{\Omega} [I(x) \cdot [1-u(x)]^m]}{\sum_{\Omega} [1-u(x)]^m}, \quad (\text{B1})$$

where  $u(x)$  is the degree of membership for pixel  $x$ , and  $I(x)$  is the corresponding intensity value.

Two average intensities  $f_b$  and  $f_s$  defined in Eq. (11) in a local image domain  $\Omega_x$  with spatial weighting coefficient  $\omega(x, y)$  are expressed in the following convolution form:

$$f_1 = \frac{\omega(x, y) * [I(x) \cdot [u(x)]^m]}{\omega(x, y) * [u(x)]^m}, \text{ and } f_2 = \frac{\omega(x, y) * [I(x) \cdot [1-u(x)]^m]}{\omega(x, y) * [1-u(x)]^m}. \quad (\text{B2})$$

For pixel  $x$ , suppose the degree of membership is  $u_0$ , the intensity value for point  $P$  is  $I_0$ , the new degree of membership is  $u_n$ . The updated membership function in Eq. (21) during each iteration is presented as  $\hat{u}(x) = \sum u_n$  and  $1 - \hat{u}(x) = \sum [1 - u_n]$ . Therefore, the new constants  $\hat{c}_1$  and  $\hat{c}_2$  are rewritten as:

$$\hat{c}_1 = \frac{\sum_{\Omega} \sum I_0 u_n^m}{\sum_{\Omega} \sum u_n^m} = \frac{\sum_{\Omega} I(x) \cdot [\hat{u}(x)]^m}{\sum_{\Omega} [\hat{u}(x)]^m} \text{ and } \hat{c}_2 = \frac{\sum_{\Omega} \sum I_0 [1 - u_n]^m}{\sum_{\Omega} \sum [1 - u_n]^m} = \frac{\sum_{\Omega} I(x) \cdot [1 - \hat{u}(x)]^m}{\sum_{\Omega} [1 - \hat{u}(x)]^m} \quad (\text{B3})$$

The new local constant  $\hat{f}_b$  is expressed as follows:

$$\begin{aligned} \hat{f}_b &= \frac{\sum_{\Omega} \sum_{\Omega_x} \sum \omega(x, y) I(y) u_n^m}{\sum_{\Omega} \sum_{\Omega_x} \sum \omega(x, y) u_n^m} = \frac{\sum_{\Omega} \sum_{\Omega_x} \omega(x, y) I(y) \sum u_n^m}{\sum_{\Omega} \sum_{\Omega_x} \omega(x, y) \sum u_n^m} \\ &= \frac{\sum_{\Omega} \sum_{\Omega_x} \omega(x, y) I(y) [\hat{u}(x)]^m}{\sum_{\Omega} \sum_{\Omega_x} \omega(x, y) [\hat{u}(x)]^m} = \frac{\sum_{\Omega} [\hat{u}(x)]^m \sum_{\Omega_x} I(y) \omega(x, y)}{\sum_{\Omega} [\hat{u}(x)]^m \sum_{\Omega_x} \omega(x, y)} \\ &= \frac{\sum_{\Omega} [\hat{u}(x)]^m * (I(x) \omega(x, y))}{\sum_{\Omega} [\hat{u}(x)]^m * (\omega(x, y))} = \frac{\sum_{\Omega} \omega(x, y) * (I(x) [\hat{u}(x)]^m)}{\sum_{\Omega} \omega(x, y) * [\hat{u}(x)]^m} \end{aligned} \quad (\text{B4})$$

In such a way, the constant  $\hat{f}_s$  can be written as:

$$\hat{f}_s = \frac{\sum_{\Omega} \sum_{\Omega_x} \omega(x, y) I(y) [1 - u_n]^m}{\sum_{\Omega} \sum_{\Omega_x} \omega(x, y) [1 - u_n]^m} = \frac{\sum_{\Omega} \omega(x, y) * (I(x) [1 - \hat{u}(x)]^m)}{\sum_{\Omega} \omega(x, y) * [1 - \hat{u}(x)]^m} \quad (\text{B5})$$

The region energy in Eq. (19) can be computed as:

$$\begin{aligned} F^R &= \lambda_1 \sum_{\Omega} [u(x)]^m g(I(x) - I(x) - (f_b + c_1)/2)^2 + \lambda_2 \sum_{\Omega} [1 - u(x)]^m g(I(x) - (f_s + c_2)/2)^2 \\ &\quad + \alpha_1 \sum_{\Omega} [u(x)]^m \left[ \sum_{\Omega} \omega(x, y) g(I(y) - f_b(x))^2 \right] \\ &\quad + \alpha_2 \sum_{\Omega} [1 - u(x)]^m \left[ \sum_{\Omega} \omega(x, y) g(I(y) - f_s(x))^2 \right] \quad , \text{with} \\ &= (E_A^{HFR} + E_B^{HFR}) + (E_C^{LFR} + E_D^{LFR}) \end{aligned}$$

$$F_A^{HFR} = \lambda_1 \sum_{\Omega} [u(x)]^m g(I(x) - (f_b + c_1)/2)^2$$

$$F_B^{HFR} = \lambda_2 \sum_{\Omega} [1 - u(x)]^m g(I(x) - (f_s + c_2)/2)^2$$

$$F_C^{LFR} = \alpha_1 \sum_{\Omega} [u(x)]^m \left[ \sum_{\Omega} \omega(x, y) g(I(y) - f_b(x))^2 \right] \quad (\text{B6})$$

$$F_D^{LFR} = \alpha_2 \sum_{\Omega} [1 - u(x)]^m \left[ \sum_{\Omega} \omega(x, y) g(I(y) - f_s(x))^2 \right]$$

The region energy of the proposed model in Eq. (B5) will change when degree of membership  $u(x)$  is changed. Let us assume the old and new region energy are  $F^R$  and  $\hat{F}^R$ , the new energy in the discrete space is written in the following form:

$$\hat{F}^R = (\hat{F}_A^{HFR} + \hat{F}_B^{HFR}) + (\hat{F}_C^{LFR} + \hat{F}_D^{LFR}) \quad (\text{B7})$$

with

$$\hat{F}_A^{HFR} = \lambda_1 \sum_{\Omega} [\hat{u}(x)]^m g(I(x) - (\hat{f}_b + \hat{c}_1)/2)^2$$

$$\hat{F}_B^{HFR} = \lambda_2 \sum_{\Omega} [1 - \hat{u}(x)]^m g(I(x) - (\hat{f}_s + \hat{c}_2)/2)^2$$

$$\hat{F}_C^{LFR} = \alpha_1 \sum_{\Omega} [\hat{u}(x)]^m \left[ \sum_{\Omega} \omega(x, y) g(I(y) - \hat{f}_b(x))^2 \right] \quad (\text{B6})$$

$$\hat{F}_D^{LFR} = \alpha_2 \sum_{\Omega} [1 - \hat{u}(x)]^m \left[ \sum_{\Omega} \omega(x, y) g(I(y) - \hat{f}_s(x))^2 \right]$$

So the alteration  $\Delta F^R$  between the new and old total energy is written as

$$\begin{aligned} \Delta F^R &= \hat{F}^R - F^R = (\hat{F}_A^{HFR} + \hat{F}_B^{HFR}) + (\hat{F}_C^{LFR} + \hat{F}_D^{LFR}) - (F_A^{HFR} + F_B^{HFR}) - (F_C^{LFR} + F_D^{LFR}) \\ &= (\hat{F}_A^{HFR} - F_A^{HFR}) + (\hat{F}_B^{HFR} - F_B^{HFR}) + (\hat{F}_C^{LFR} - F_C^{LFR}) + (\hat{F}_D^{LFR} - F_D^{LFR}) \quad (\text{B7}) \end{aligned}$$

## Appendix C. Supplementary data

Supplementary data to this article can be found online at <https://doi.org/10.1016/j.ins.2020.08.078>.

## References

- [1] D. Cremers, M. Rousson, R. Deriche, A review of statistical approaches to level set segmentation: integrating color texture, motion and shape, *Int. J. Comput. Vis.* 72 (5) (2007) 195–215.
- [2] X. Munoz, J. Freixenet, X. Cufi, J. Marti, Strategies for image segmentation combining region and boundary information, *Pattern Recognit.* 24 (1) (2003) 375–392.
- [3] S. Kim, S. Nowozin, P. Kohli, D.Y. Chang, Higher-order correlation clustering for image segmentation, *IEEE Trans. Pattern Anal. Mach. Intell.* 36 (2015) 1761–1774.
- [4] M. Kass, A. Witkin, D. Terzopoulos, Snakes: active contour models, *Int. J. Comput. Vis.* 1 (1988) 321–331.
- [5] V. Caselles, R. Kimmel, G. Sapiro, Geodesic active contours, *Int. J. Comput. Vis.* 22 (1997) 61–79.
- [6] T. Chan, L. Vese, Active contours without edges, *IEEE Trans. Image Proc.* 10 (2001) 266–277.
- [7] S.C. Zhu, A. Yuille, Region competition: Unifying snakes, region growing, and Bayes/MDL for multiband image segmentation, *IEEE Trans. Pattern Anal. Mach. Intell.* 18 (9) (1996) 884–900.
- [8] D. Mumford, J. Shah, Optimal approximation by piecewise smooth functions and associated variational problems, *Commun. Pure Appl. Math.* 42 (1989) 577–685.

- [9] C. Li, C. Y. Kao, J.C. Gore, Z. Ding, Implicit active contours driven by local binary fitting energy, IEEE Conf. Comput. Vis. Pattern Recognit. 7 (2007) Minneapolis.
- [10] L. Vese, T. Chan, A multiphase level set framework for image segmentation using the Mumford and Shah model, Int. J. Comput. Vis. 50 (2002) 271–293.
- [11] C. Li, C.Y. Kao, J.C. Gore, Z. Ding, Minimization of region-scalable fitting energy for image segmentation, IEEE Trans. Image Proc. 17 (2008) 1940–1949.
- [12] K. Zhang, H. Song, L. Zhang, Active contours driven by local image fitting energy, Pattern Recognit. 43 (4) (2010) 1199–1206.
- [13] L. Wang, Y. Chang, H. Wang, Z.Z. Wu, J.T. Pu, X.D. Yang, An active contour model based on local fitted images for image segmentation, Inf. Sci. 418–419 (2017) 61–73.
- [14] Z.X. Jia, Y. Xia, Q.S. Sun, G. Cao, Q. Chen, Active contours driven by local likelihood image fitting energy for image segmentation, Inf. Sci. 301 (2015) 285–304.
- [15] J.Q. Miao, T.Z. Huang, X.B. Zhou, Y.G. Wang, J. Liu, Image segmentation based on an active contour model of partial image restoration with local cosine fitting energy, Inf. Sci. 418–419 (2017) 61–73.
- [16] K.Y. Ding, L.F. Xiao, G.R. Weng, Active contours driven by local pre-fitting energy for fast image segmentation, Pattern Recognit. Lett. 104 (2018) 29–36.
- [17] X. Wang, D. Huang, H. Xu, An efficient local Chan-Vese model for image segmentation, Pattern Recognit. 43 (3) (2010) 603–618.
- [18] C.J. He, Y. Wang, Q. Chen, Active contours driven by weighted region-scalable fitting energy based on local entropy, Signal Process. 92 (2012) 587–600.
- [19] T. Brox, D. Cremers, On local region models and a statistical interpretation of the piecewise smooth Mumford-Shah functional, Int. J. Comput. Vis. 84 (2009) 184–193.
- [20] H. Wang, M. Liu, Active contours driven by local Gaussian distribution fitting energy based on local entropy, Int. J. Pattern Recognit. Artif. Intell. 27 (6) (2013) 1073–1089.
- [21] H. Ali, N. Badshah, K. Chen, G. Khan, A variational model with hybrid images data fitting energies for segmentation of images with intensity inhomogeneity, Pattern Recognit. 51 (2016) 27–42.
- [22] C. Li, C. Xu, C. Gui, M.D. Fox, Level set evolution without re-initialization: a new variational formulation, IEEE Conf. Comput. Vis. Pattern Recognit. (CVPR) 1 (2005) 430–436.
- [23] C. Li, C. Xu, C. Gui, M.D. Fox, Distance regularized level set evolution and its application to image segmentation, IEEE Trans. Image Process. 19 (12) (2010) 3243–3254.
- [24] S. Krinidis, V. Chatzis, Fuzzy energy-based active contour, IEEE Trans. Image Process. 18 (12) (2009) 2747–2755.
- [25] K. Shyu, V. Pham, T. Tran, P. Lee, Global and local fuzzy energy-based active contours for image segmentation, Nonlinear Dynam. 67 (2) (2012) 1559–1578.
- [26] A. Mondal, S. Ghosh, A. Ghosh, Robust global and local fuzzy energy based active contour for image segmentation, Appl. Soft Comput. 47 (2016) 191–215.
- [27] A. Mondal, S. Ghosh, A. Ghosh, Partially camouflaged object tracking using modified probabilistic neural network and fuzzy energy based active contour, Int. J. Comput. Vis. 122 (2017) 116–148.
- [28] W.Y. Sun, E.Q. Dong, H.J. Qiao, A fuzzy energy-based active contour model with adaptive contrast constraint for local segmentation, SIViP 12 (1) (2018) 91–98.
- [29] T.T. Tran, V.T. Pham, K.K. Shyu, Image segmentation using fuzzy energy-based active contour with shape prior, J. Vis. Commun. Image R. 25 (2014) 1732–1745.
- [30] K. Zhang, L. Zhang, H. Song, W. Zhou, Active contours with selective local or global segmentation: a new formulation and level set method, Image Vision Comput. 28 (4) (2010) 668–676.
- [31] X. Shan, D. Kim, E. Kobayashi, B.N. Li, Regularized level set models using fuzzy clustering for medical image segmentation, Filomat 32 (5) (2018) 1507–1512.
- [32] K. Hanbay, M.F. Talu, A novel active contour model for medical images via the Hessian matrix and eigenvalues, Comput. Math. Appl. 75 (2018) 3081–3104.
- [33] J. Fang, H. Liu, L. Zhang, J. Liu, H. Liu, Fuzzy region-based active contours driven by weighting global and local fitting energy, IEEE Access (2019) 184518–184536.
- [34] J. Fang, H. Liu, L. Zhang, J. Liu, H. Liu, Active contour driven by weighted hybrid signed pressure force for image segmentation, IEEE Access (2019) 97492–97504.
- [35] H. Zhang, J.E. Fritts, S.A. Goldman, An entropy-based objective evaluation method for image segmentation, Electron. Imag. (2003) 38–49.
- [36] T. Liu, J. Sun, N.N. Zheng, X. Tang, H.Y. Shum, Learning to detect a salient object, IEEE CVPR (2007).
- [37] M.B. Salah, A. Mitiche, I.B. Ayed, Efficient level set segmentation with a kernel induced data term, IEEE Trans. Image Proc. 19 (2010) 220–232.



**Jiangxiang Fang** received the Ph.D degree in pattern recognition and intelligent system at the Institute of Image Processing and Pattern Recognition from Shanghai JiaoTong University, shanghai, China, in 2012, and the BS and MS from Central South University, Changsha, China, in 2004 and 2007, respectively. Now, he is an associate professor as a teacher at East China University of Technology. His research interests include image segmentation, and machine learning.



**Huaxiang Liu** received the B.S. and M.S. degrees in circuits and systems from Hunan Normal University in 2007 and 2010, respectively. She is currently a teacher at East China University of Technology. Her research interests include deep learning, medical image segmentation, variational theory for image segmentation, visual object tracking and detection.



**Liting Zhang** received the Ph.D degree in cartography and geographic information engineering from Wuhan University, Wuhan, China, in 2006, and MS from East China of Technology, Fuzhou, China, in 1990, and the BS from Hefei University of Technology, Hefei, in 1999.. His research interests include remote image processing and GIS theory and application.



**Jun Liu** received the Ph.D degree in detection technology and automation devices from Northeastern University, Shenyang, China, in 2010, and the BS and MS degrees from Shenyang University of Technology, Shenyang, China, in 2003 and 2006, respectively. His research interests include metallurgical parameters detection and image processing.



**Hesheng Liu** received the Ph.D, MS and BS degrees from Shanghai JiaoTong University, from 1981 to 1990, Shanghai, China. He was selected as the *New Century National Hundred, Thousand and Ten Thousand Talent Project* in China and *Special allowance of the State Council*. Presently he is a professor and serving as president of East China University of Technology. His research interests include mechanical and electrical integration, advanced control systems and optimization algorithm.